

# The supernova-regulated ISM. I. The multi-phase structure

F. A. Gent,<sup>1,4,\*</sup> A. Shukurov,<sup>1</sup> A. Fletcher,<sup>1</sup> G. R. Sarson,<sup>1</sup> M. J. Mantere<sup>2,3</sup>

<sup>1</sup>*School of Mathematics and Statistics, Newcastle University, Newcastle upon Tyne NE1 7RU, UK*

<sup>2</sup>*Physics Department, University of Helsinki, PO BOX 64, Helsinki, FI-00014, Finland*

<sup>3</sup>*Department of Information and Computer Science, Aalto University, PO Box 15400, FI-00076 Aalto, Finland*

<sup>4</sup>*School of Mathematics and Statistics, University of Sheffield, Sheffield S3 7RH, UK*

28 May 2022

## ABSTRACT

We simulate the multi-phase interstellar medium (ISM) randomly heated and stirred by supernovae (SNe), with gravity, differential rotation and other parameters of the solar neighbourhood. Here we describe in detail both numerical and physical aspects of the model, including injection of thermal and kinetic energy by SN explosions, radiative cooling, photo-electric heating and various transport processes. With a three-dimensional domain extending  $1 \times 1 \text{ kpc}^2$  horizontally and  $2 \text{ kpc}$  vertically (symmetric about the galactic mid-plane), the model routinely spans gas number densities  $10^{-5}$ – $10^2 \text{ cm}^{-3}$ , temperatures  $10$ – $10^8 \text{ K}$ , local velocities up to  $10^3 \text{ km s}^{-1}$  (with Mach number up to 25). The working numerical resolution of  $4 \text{ pc}$  has been selected via simulations of a single expanding SN remnant, where we closely reproduce, at this resolution, analytical solutions for the adiabatic and snowplough regimes. The feedback of the the halo on the disc cannot be captured in our model where the domain only extends to the height of  $1 \text{ kpc}$  above the mid-plane. We argue that to reliably model the disc-halo connections would require extending the domain horizontally as well as vertically due to the increasing horizontal scale of the gas flows with height.

The thermal structure of the modelled ISM is classified by inspection of the joint probability density of the gas number density and temperature. We confirm that most of the complexity can be captured in terms of just three phases, separated by temperature borderlines at about  $10^3 \text{ K}$  and  $5 \times 10^5 \text{ K}$ . The probability distribution of gas density within each phase is approximately lognormal. We clarify the connection between the fractional volume of a phase and its various proxies, and derive an exact relation between the fractional volume and the filling factors defined in terms of the volume and probabilistic averages. These results are discussed in both observational and computational contexts. The correlation scale of the random flows is calculated from the velocity autocorrelation function; it is of order  $100 \text{ pc}$  and tends to grow with distance from the mid-plane. We use two distinct parameterizations of radiative cooling to show that the multi-phase structure of the gas is robust, as it does not depend significantly on this choice.

**Key words:** galaxies: ISM – ISM: kinematics and dynamics – turbulence

## 1 INTRODUCTION

The multi-phase structure of the interstellar medium (ISM) affects almost all aspects of its dynamics, including its evolution, star formation, galactic winds and fountains, and the behaviour of magnetic fields and cosmic rays. In a widely accepted picture (Cox & Smith 1974; McKee & Ostriker 1977), most of the volume is occupied by the hot ( $T \simeq 10^6 \text{ K}$ ), warm ( $T \simeq 10^4 \text{ K}$ ) and cold ( $T \simeq 10^2 \text{ K}$ ) phases. The concept of the multi-phase ISM in pressure equilibrium has endured with modest refinement (Cox 2005),

e.g., deviations from thermal pressure balance have been detected (Kalberla & Kerp 2009, and references therein). Dense molecular clouds, while binding most of the total mass of the interstellar gas and being of key importance for star formation, occupy a negligible fraction of the total volume (e.g. Kulkarni & Heiles 1987, 1988; Spitzer 1990; McKee 1995). The main sources of energy maintaining this complex structure are supernova (SN) explosions and stellar winds (Mac Low & Klessen 2004, and references therein). The clustering of SNe in OB associations facilitates the escape of the hot gas into the halo thus reducing the volume filling factor of the hot gas in the disc, perhaps down to 10% at the mid-plane (Norman & Ikeuchi 1989). The energy injected by the SNe not only produces the hot gas but also drives ubiquitous compressible turbulence in all phases, as well as driving outflows from the disc, associated with

\* E-mails: F.Gent@sheffield.ac.uk, Anvar.Shukurov@ncl.ac.uk,  
Andrew.Fletcher@ncl.ac.uk, G.R.Sarson@ncl.ac.uk and  
Maarit.Mantere@helsinki.fi

the galactic fountain or wind, as first suggested by Bregman (1980). Thus turbulence, the multi-phase structure, and the disc-halo connection are intrinsically related features of the ISM.

A comprehensive description of the complex dynamics of the multi-phase ISM has been significantly advanced by numerical simulations in the last three decades, starting with Chiang & Prendergast (1985), followed by many others including Rosen et al. (1993); Rosen & Bregman (1995); Vázquez-Semadeni et al. (1995); Passot et al. (1995); Rosen et al. (1996); Korpi et al. (1999); Gazol-Patiño & Passot (1999); Wada & Norman (1999); de Avillez (2000); Wada & Norman (2001); de Avillez & Berry (2001); de Avillez & Mac Low (2002); Wada et al. (2002); de Avillez & Breitschwerdt (2004); Balsara et al. (2004); de Avillez & Breitschwerdt (2005a); de Avillez & Breitschwerdt (2005b); Slyz et al. (2005); Mac Low et al. (2005); Joung & Mac Low (2006); de Avillez & Breitschwerdt (2007); Wada & Norman (2007); Gressel et al. (2008). Numerical simulations of this type are demanding even with the best computers and numerical methods available. The self-regulation cycle of the ISM includes physical processes spanning enormous ranges of gas temperature and density, and of spatial and temporal scales, as it involves star formation in the cores of molecular clouds, assisted by gravitational and thermal instabilities at larger scales, which evolve against the global background of transonic turbulence driven, in turn, by star formation (Mac Low & Klessen 2004). It is understandable that none of the existing numerical models covers the whole range of parameters, scales and physical processes known to be important.

Two major approaches in earlier work focus either on the dynamics of diffuse gas or on dense molecular clouds. Our model belongs to the former class, where we are mainly concerned with the ISM dynamics in the range of scales of order 10 pc–1 kpc. Numerical constraints prevent us (like many other authors) from fully including the gravitational and thermal instabilities which involve scales of less than 1 pc. In order to assess the sensitivity of our results to the parameterization of radiative cooling, we consider models with thermal instability, but reduce its efficiency using a sufficiently strong thermal conductivity to avoid the emergence of structures that are unresolvable at our numerical resolution. The results are compared to models with no thermally unstable branch over the temperature range between the cold and warm phases. To our knowledge, no direct study addressing the difference between these two kinds of the cooling parameterizations has been made. We note, however, that Vázquez-Semadeni et al. (2000) compared their thermally unstable model to a different model by Scalo et al. (1998), who used a thermally stable cooling function. Similarly, de Avillez & Breitschwerdt (2004) and Joung & Mac Low (2006) compared results obtained with different cooling functions, but again comparing different models: here we compare models with different cooling functions but which are otherwise the same.

An unavoidable consequence of the modest numerical resolution available, if we are to capture the dynamics on 1 kpc scales, is that star formation, manifesting itself only through the ongoing SN activity in our model, has to be heavily parameterized. We do, however, ensure that individual supernova remnants are modelled accurately, since this is essential to reliably reproduce the injection of thermal and kinetic energy into the ISM. In particular, our model reproduces with high accuracy the evolution of supernova remnants from the Sedov–Taylor stage until the remnant disintegrates and merges into the ISM (Appendix B).

The dimensionless parameters characteristic of the ISM, such as the kinetic and magnetic Reynolds numbers (reflecting the relative importance of gas viscosity and electrical resistivity) and the

Prandtl number (quantifying thermal conductivity), are too large to be simulated with current computers. Similarly to most numerical simulations of this complexity, our numerical techniques involve a range of artificial transport coefficients for momentum and thermal energy (such as shock-capturing viscosity). We explore and report here the sensitivity of our results to the artificial elements in our basic equations.

This paper is the first of a planned series, in which we aim to clarify which components and physical processes control the different properties of the ISM. Our next step is to add magnetic fields to the model, to study both their origin and role in shaping the ISM. But in order to identify where the magnetic field is important and where it is not, we first must understand what the properties of a purely hydrodynamic ISM would be.

The structure of the paper is as follows. In Section 2 we present our basic equations, numerical methods, initial and boundary conditions, as well as the physical ingredients of the model, such as our modelling of SN activity and heating and cooling of the ISM. Our results are presented in Sections 3–8, including an overview of the multi-phase structure of the ISM, the correlation length of random flows, and their sensitivity to the cooling function and numerical resolution. Our results are discussed in a broader context in Section 9, where our conclusions are also summarised. Detailed discussion of important technical and numerical aspects of the model, and the effects of the unavoidable unphysical assumptions adopted, can be found in Appendices: the accuracy of our modelling of individual supernova remnants in Appendix B, our control of numerical dissipation in Appendix C, and sensitivity to thermal instability in Appendix D.

## 2 BASIC EQUATIONS AND THEIR NUMERICAL IMPLEMENTATION

### 2.1 Basic equations

We solve numerically a system of hydrodynamic equations using the PENCIL CODE (<http://code.google.com/p/pencil-code>) which is designed for fully nonlinear, compressible magnetohydrodynamic (MHD) simulations. We consider only the hydrodynamic regime for the purposes of this paper; MHD simulations, which are in progress, will be reported elsewhere. Nor do we include cosmic rays, which we subsequently plan to add to the MHD simulations.

The basic equations include the mass conservation equation, the Navier–Stokes equation (written here in the rotating frame), and the heat equation written in terms of the specific entropy:<sup>1</sup>

$$\begin{aligned} \frac{D\rho}{Dt} &= -\rho \nabla \cdot \mathbf{u} + \dot{\rho}_{\text{SN}}, & (1) \\ \frac{D\mathbf{u}}{Dt} &= -\rho^{-1} \nabla \sigma_{\text{SN}} - c_s^2 \nabla (s/c_p + \ln \rho) \\ &\quad - \nabla \Phi - S_{u,x} \hat{\mathbf{y}} - 2\boldsymbol{\Omega} \times \mathbf{u} \\ &\quad + \nu (\nabla^2 \mathbf{u} + \frac{1}{3} \nabla \nabla \cdot \mathbf{u} + 2\mathbf{W} \cdot \nabla \ln \rho) \\ &\quad + \zeta_\nu (\nabla \nabla \cdot \mathbf{u}), & (2) \\ \rho T \frac{Ds}{Dt} &= \dot{\sigma}_{\text{SN}} + \rho \Gamma - \rho^2 \Lambda + \nabla \cdot (c_p \rho \chi \nabla T) + 2\rho \nu |\mathbf{W}|^2 \\ &\quad + \zeta_\chi \rho (\nabla \cdot \mathbf{u})^2, & (3) \end{aligned}$$

<sup>1</sup> For the reader's convenience, Appendix A contains a list of variables used in the text with their definitions.

where  $\rho$ ,  $T$  and  $s$  are the gas density, temperature and specific entropy, respectively,  $\mathbf{u}$  is the deviation of the gas velocity from the background rotation profile (here called the *velocity perturbation*),  $c_s$  is the adiabatic speed of sound,  $c_p$  is the heat capacity at constant pressure,  $S$  is the velocity shear rate associated with the Galactic differential rotation at the angular velocity  $\Omega$  assumed to be aligned with the  $z$ -axis (see below). The Navier–Stokes equation includes viscosity  $\nu$  and the rate of strain tensor  $\mathbf{W}$  whose components are given by

$$2W_{ij} = \frac{\partial u_i}{\partial x_j} + \frac{\partial u_j}{\partial x_i} - \frac{2}{3}\delta_{ij}\nabla \cdot \mathbf{u}, \quad (4)$$

as well as the shock-capturing viscosity  $\zeta\nu$ . The system is driven by SN energy injection, at the rates  $\dot{\sigma}_{\text{SN}}$  (per unit volume) in the form of kinetic energy in Eq. (2) and thermal energy in Eq. (3). Energy injection is applied in a single time step and is confined to the interiors of newly introduced SN remnants, and the total energy injected per supernova is denoted  $E_{\text{SN}}$ . The mass of the SN ejecta is included in Eq. (1) via the source  $\dot{\rho}_{\text{SN}}$ . The forms of these terms are specified and further details are given in Section 2.2. The heat equation also contains a thermal energy source due to photoelectric heating  $\rho\Gamma$ , energy loss due to optically thin radiative cooling  $\rho^2\Lambda$ , heat conduction with the thermal diffusivity  $\chi$  (with  $K = c_p\rho\chi$  the thermal conductivity), viscous heating (with  $|\mathbf{W}|$  the determinant of  $\mathbf{W}$ ), and the shock-capturing thermal diffusivity  $\zeta\chi$ .

The advective derivative,

$$\frac{D}{Dt} = \frac{\partial}{\partial t} + (\mathbf{U} + \mathbf{u}) \cdot \nabla, \quad (5)$$

includes transport by an imposed shear flow  $\mathbf{U} = (0, Sx, 0)$  in the local Cartesian coordinates (taken to be linear across the local simulation box), with the velocity  $\mathbf{u}$  representing a deviation from the overall rotational velocity  $\mathbf{U}$ . As will be discussed later, due to anisotropies (e.g. density stratification, anisotropic turbulence), large-scale flows will be generated in the system; one example is the systematic vertical outflow discussed at length in this paper. Therefore, the perturbation velocity  $\mathbf{u}$  consists of two parts, a mean flow and random velocities. Here we consider a mean flow obtained by Gaussian smoothing (Germano 1992):

$$\langle \mathbf{u} \rangle_{\ell}(\mathbf{x}) = \int_{\mathcal{V}} \mathbf{u}(\mathbf{x}') G_{\ell}(\mathbf{x} - \mathbf{x}') d^3\mathbf{x}', \quad (6)$$

$$G_{\ell}(\mathbf{x}) = (2\pi\ell^2)^{-3/2} \exp[-\mathbf{x}^2/(2\ell^2)],$$

where we use a smoothing scale  $\ell \simeq 50$  pc, necessarily somewhat shorter than the flow correlation length  $l_0$  obtained in Section 6 (for details, see Gent et al. 2013). The random flow is then  $\mathbf{u}_0 = \mathbf{u} - \langle \mathbf{u} \rangle_{\ell}$ . The differential rotation of the galaxy is modelled with a background shear flow along the local azimuthal ( $y$ ) direction,  $U_y = Sx$ . The shear rate is  $S = r\partial\Omega/\partial r$  in terms of galactocentric distance  $r$ , which translates into the  $x$ -coordinate of the local Cartesian frame. In this paper we consider models with rotation and shear similar to those in the solar neighbourhood,  $\Omega = -S = 25 \text{ km s}^{-1} \text{ kpc}^{-1}$ . We do not expect the gas velocities and thermal structure discussed here to depend strongly on the rotation and shear parameters, although other aspects of the solution will be more sensitive to these. Future papers will consider the rotation and shear in more detail; and will also include magnetic fields, whose generation may depend strongly on these parameters.

We consider an ideal gas, with thermal pressure given by

$$p = \frac{k_B}{\mu m_p} \rho T,$$

where  $k_B$  is the Boltzmann constant,  $m_p$  is the proton mass, and

$\mu = 0.62$  is the mean molecular weight of a fully ionised gas of the Solar chemical composition.

In Eq. (2),  $\Phi$  is the gravitational potential produced by stars and dark matter. For the Solar vicinity of the Milky Way, Kuijken & Gilmore (1989) suggest the following form of the vertical gravitational acceleration (see also Ferrière 2001):

$$g_z = -\frac{\partial\Phi}{\partial z} = -\frac{a_1}{\sqrt{z_1^2 + z^2}} - a_2 \frac{z}{z_2}, \quad (7)$$

with  $a_1 = 4.4 \times 10^{-16} \text{ km s}^{-2}$ ,  $a_2 = 1.7 \times 10^{-16} \text{ km s}^{-2}$ ,  $z_1 = 200$  pc and  $z_2 = 1$  kpc. We neglect self-gravity of the interstellar gas because it is subdominant at the scales of interest.

## 2.2 Modelling supernova activity

We include both Type II and Type I SNe in our simulations, distinguished only by their frequency and vertical distribution. The SNe frequencies are those in the Solar neighbourhood (e.g. Tammann, Löffler & Schröder 1994). Type II SNe are introduced at a rate, per unit surface area, of  $\nu_{\text{II}} = 25 \text{ kpc}^{-2} \text{ Myr}^{-1}$  ( $0.02 \text{ yr}^{-1}$  in the whole Galaxy), with fluctuations of the order of  $10^{-4} \text{ yr}^{-1}$  at a time scale of order 10 Myr. Such fluctuations in the Type II SN rate are natural to introduce; there is some evidence that they can enhance dynamo action in MHD models (Hanasz et al. 2004; Balsara et al. 2004). The surface density rate of Type I SNe is  $\nu_{\text{I}} = 4 \text{ kpc}^{-2} \text{ Myr}^{-1}$  (interval of 290 years between Type I SN explosions in the Galaxy). We do not explicitly include any spatial clustering of the SNe.

Unlike most other ISM models of this type, the SN energy in the injection site is split between thermal and kinetic parts, in order to reduce artificial temperature and energy losses at early stages of the SN remnant evolution. Thermal energy density is distributed within the injection site as  $\exp[-(r/r_{\text{SN}})^6]$ , with  $r$  the local spherical radius and  $r_{\text{SN}}$  (of order 10 pc – see below) the nominal location of the remnant shell (i.e. the radius of the SN bubble) at the time of injection. Kinetic energy is injected by adding a spherically symmetric velocity field  $u_r \propto \exp[-(r/r_{\text{SN}})^6]$ ; subsequently, this rapidly redistributes matter into a shell. To avoid a discontinuity in  $\mathbf{u}$  at the centre of the injection site, the centre is simply placed midway between grid points. We also inject  $4M_{\odot}$  as stellar ejecta, with density profile  $\exp[-(r/r_{\text{SN}})^6]$ . Given the turbulent environment, there are significant random motions and density inhomogeneities within the injection regions. Thus, the initial kinetic energy is not the same in each region, and, injecting part of the SN energy in the kinetic form results in the total kinetic energy varying between SN remnants. We therefore record the energy added for every remnant so we can fully account with the rate of energy injection. For example, in Model WSWa we obtain the energy per SN in the range

$$0.5 < E_{\text{SN}} < 1.5 \times 10^{51} \text{ erg},$$

with the average of  $0.9 \times 10^{51}$  erg.

The SN sites are randomly distributed in the horizontal coordinates ( $x, y$ ). Their vertical positions are drawn from the Gaussian distributions in  $z$  with the scale heights of  $h_{\text{II}} = 0.09$  kpc for Type II and  $h_{\text{I}} = 0.325$  kpc for Type I SNe. Thus, Eq. (1) contains the mass source of  $4M_{\odot}$  per SN,

$$\dot{\rho}_{\text{SN}} \simeq 4M_{\odot} \left( \frac{\nu_{\text{II}}}{2h_{\text{II}}} + \frac{\nu_{\text{I}}}{2h_{\text{I}}} \right),$$

whereas Eqs. (2) and (3) include kinetic and thermal energy sources

of similar strength adding up to  $E_{\text{SN}}$  per SN:

$$\dot{\sigma}_{\text{SN}} \simeq \frac{1}{2} E_{\text{SN}} \left( \frac{\nu_{\text{II}}}{2h_{\text{II}}} + \frac{\nu_{\text{I}}}{2h_{\text{I}}} \right).$$

The only other constraints applied when choosing SN sites are to reject a site if an SN explosion would result in a local temperature above  $10^{10}$  K or if the local gas number density exceeds  $2 \text{ cm}^{-3}$ . The latter requirement ensures that the thermal energy injected is not lost to radiative cooling before it can be converted into kinetic energy in the ambient gas. More elaborate prescriptions can be suggested to select SN sites (Korpi et al. 1999; de Avillez 2000; Joung & Mac Low 2006; Gressel et al. 2008); we found this unnecessary for our present purposes.

Arguably the most important feature of SN activity, in the present context, is the efficiency of evolution of the SN energy from thermal to kinetic energy in the ISM, a transfer that occurs via the shocked, dense shells of SN remnants. Given the relatively low resolution of this model (and most, if not all, other models of this kind), it is essential to verify that the dynamics of expanding SN shells is captured correctly: inaccuracies in the SN remnant evolution would indicate that our modelling of the thermal and kinetic energy processes was unreliable. Therefore, we present in Appendix B detailed numerical simulations of the dynamical evolution of an individual SN remnant at spatial grid resolutions in the range  $\Delta = 1\text{--}4$  pc. We allow the SN remnant to evolve from the Sedov–Taylor stage (at which SN remnants are introduced in our simulations) for  $t \approx 3.5$  Myr. The remnant enters the snow-plough regime, with a final shell radius exceeding 100 pc, and we compare the numerical results with the analytical solution of Cioffi et al. (1998). The accuracy of the numerical results depends on the ambient gas density  $n_0$ : larger  $n_0$  requires higher resolution to reproduce the analytical results. We show that agreement with Cioffi et al. (1998) in terms of the shell radius and expansion speed is excellent at resolutions  $\Delta \leq 2$  pc for  $n_0 \simeq 1 \text{ cm}^{-3}$ , and also very good at  $\Delta = 4$  pc for  $n_0 \approx 0.1$  and  $0.01 \text{ cm}^{-3}$ . Comparisons with models of higher resolution (de Avillez & Breitschwerdt 2004; Joung et al. 2009), in Section 8.3, also indicate that our basic  $\Delta = 4$  pc resolution is adequate.

Since shock waves in the immediate vicinity of an SN site are usually stronger than anywhere else in the ISM, these tests also confirm that our handling of shock fronts is sufficiently accurate and that the shock-capturing diffusivities that we employ do not unreasonably affect the shock evolution.

Our standard resolution is  $\Delta = 4$  pc. To be minimally resolved, the initial radius of an SN remnant must span at least two grid points. Because the origin is set between grid points, a minimum radius of 7 pc for the energy injection site is sufficient. The size of the energy injection region in our model must be such that the gas temperature is above  $10^6$  K and below  $10^8$  K: at both higher and lower temperatures, energy losses to radiation are excessive and adiabatic expansion cannot be established. Following Joung & Mac Low (2006), we adjust the radius of the energy injection region to be such that it contains  $60M_{\odot}$  of gas. For example, in model WSWa this results in a mean  $r_{\text{SN}}$  of 35 pc, with a standard deviation of 25 pc and a maximum of 200 pc. The distribution of radii appears approximately lognormal, so  $r_{\text{SN}} > 75$  pc is very infrequent and the modal value is about 10 pc; this corresponds to the middle of the Sedov–Taylor phase of the SN expansion. Unlike Joung & Mac Low (2006), we found that mass redistribution within the injection site was not necessary. Therefore we do not impose uniform site density, particularly as it may lead to unexpected

**Table 1.** The cooling function of Wolfire et al. (1995) at  $T < 10^5$  K, joined to that of Sarazin & White (1987) at higher temperatures, with  $\Lambda = 0$  for  $T < 10$  K. This cooling function is denoted WSW in the text (and in the labels of our numerical models).

$T_k$ [K]	$\Lambda_k$ [erg g $^{-2}$ s $^{-1}$ cm $^3$ K $^{-\beta_k}$ ]	$\beta_k$
10	$3.70 \times 10^{16}$	2.12
141	$9.46 \times 10^{18}$	1.00
313	$1.18 \times 10^{20}$	0.56
6102	$1.10 \times 10^{10}$	3.21
$10^5$	$1.24 \times 10^{27}$	−0.20
$2.88 \times 10^5$	$2.39 \times 10^{42}$	−3.00
$4.73 \times 10^5$	$4.00 \times 10^{26}$	−0.22
$2.11 \times 10^6$	$1.53 \times 10^{44}$	−3.00
$3.98 \times 10^6$	$1.61 \times 10^{22}$	0.33
$2.00 \times 10^7$	$9.23 \times 10^{20}$	0.50

**Table 2.** The cooling function of Rosen et al. (1993), labelled RBN in the text (and in the labels of our numerical models), with  $\Lambda = 0$  for  $T < 10$  K.

$T_k$ [K]	$\Lambda_k$ [erg g $^{-2}$ s $^{-1}$ cm $^3$ K $^{-\beta_k}$ ]	$\beta_k$
10	$9.88 \times 10^5$	6.000
300	$8.36 \times 10^{15}$	2.000
2000	$3.80 \times 10^{17}$	1.500
8000	$1.76 \times 10^{12}$	2.867
$10^5$	$6.76 \times 10^{29}$	−0.650
$10^6$	$8.51 \times 10^{22}$	0.500

consequences in the presence of magnetic fields in our MHD simulations (described elsewhere).

### 2.3 Radiative cooling and photoelectric heating

We consider two different parameterizations of the optically thin radiative cooling appearing in Eq. (3), both of the piecewise power-law form  $\Lambda = \Lambda_k T^{\beta_k}$  within a number of temperature ranges  $T_k \leq T < T_{k+1}$ , with  $T_k$  and  $\Lambda_k$  given in Tables 1 and 2. Since this is just a crude (but convenient) parameterization of numerous processes of recombination and ionisation of various species in the ISM, there are several approximations designed to describe the variety of physical conditions in the ISM. Each of the earlier models of the SN-driven ISM adopts a specific cooling curve, often without explaining the reason for the particular choice or assessing its consequences. In this paper, we discuss the sensitivity of the results to the choice of the cooling function.

One parameterization of radiative cooling, labelled WSW and shown in Table 1, consists of two parts. For  $T < 10^5$  K, we use the cooling function fitted by Sánchez-Salcedo et al. (2002) to the ‘standard’ equilibrium pressure–density relation of Wolfire et al. (1995, cf. Fig. 3b therein). For higher temperatures, we adopt the cooling function of Sarazin & White (1987). This part of the cooling function (but extended differently to lower temperatures) was used by Slyz et al. (2005) to study star formation in the ISM. The WSW cooling function was also used by Gressel et al. (2008). It has two thermally unstable ranges: at  $313 \leq T < 6102$  K, the gas is isobarically unstable ( $\beta_k < 1$ ); at  $T > 10^5$  K, gas is isochorically or isentropically unstable ( $\beta_k < 0$  and  $\beta_k < -1.5$ , respectively).

Results obtained with the WSW cooling function are compared with those using the cooling function of Rosen et al. (1993), labelled RBN, whose parameters are shown in Table 2. This cool-

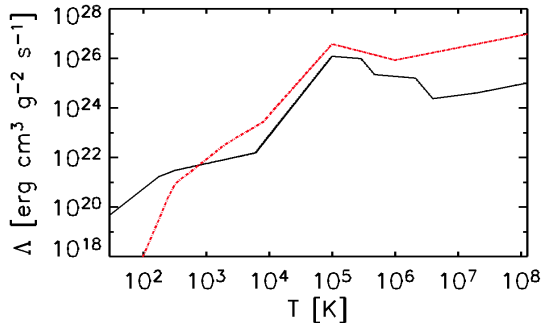


**Figure 1.** The cooling functions WSW (solid, black) and RBN (red, dash-dotted), with parameters given in Tables 1 and 2, respectively.

ing function has a thermally unstable part only above  $10^5$  K. Rosen et al. (1993) truncated their cooling function at  $T = 300$  K. Instead of abrupt truncation, we have smoothly extended the cooling function down to 10 K. This has no palpable physical consequences as the radiative cooling time at these low temperatures becomes longer (10 Myr) than other time scales in the model, so that adiabatic cooling dominates. The minimum temperature reported in the model of Rosen et al. (1993) is about 100 K. Here, with better spatial resolution, the lowest temperature is typically below 50 K.

We took special care to accurately ensure the continuity of the cooling functions, as small discontinuities may affect the performance of the code; hence the values of  $\Lambda_k$  in Table 1 differ slightly from those given by Sánchez-Salcedo et al. (2002). The two cooling functions are shown in Fig. 1. The cooling function used in each numerical model is identified with a prefix RBN or WSW in the model label (see Table 3). The purpose of Models RBN and WSWb is to assess the impact of the choice of the cooling function on the results (Section 8.1). Other models employ the WSW cooling function.

We also include photoelectric heating in Eq. (3) via the stellar far-ultraviolet (UV) radiation,  $\Gamma$ , following Wolfire et al. (1995) and allowing for its decline away from the Galactic mid-plane with a length scale comparable to the scale height of the stellar disc near the Sun (cf. Joungh & Mac Low 2006):

$$\Gamma(z) = \Gamma_0 \exp(-|z|/300 \text{ pc}), \quad \Gamma_0 = 0.0147 \text{ erg g}^{-1} \text{ s}^{-1}.$$

This heating mechanism is smoothly suppressed at  $T > 2 \times 10^4$  K, since the photoelectric effect due to UV photon impact on PAHs (Polycyclic Aromatic Hydrocarbons) and small dust grains is impeded at high temperatures (cf. Wolfire et al. 1995).

## 2.4 Numerical methods

### 2.4.1 The computational domain

We model a relatively small region within the galactic disc and lower halo with parameters typical of the solar neighbourhood. Using a three-dimensional Cartesian grid, our results have been obtained for a region  $1.024 \times 1.024 \times 2.24 \text{ kpc}^3$  in size, with 1.024 kpc in the radial and azimuthal directions and 1.12 kpc vertically on either side of the galactic mid-plane. Assuming that the correlation length of the interstellar turbulence is  $l_0 \simeq 0.1$  kpc (see Section 6), the computational domain encompasses about 2,000 turbulent cells, so the statistical properties of the ISM can be reliably captured. We are confident that our computational domain is sufficiently broad to accommodate comfortably even the largest SN

remnants at large heights, so as to exclude any self-interaction of expanding remnants through the periodic boundaries.

Vertically, our reference model accommodates ten scale heights of the cold HI gas, two scale heights of diffuse HI (the Lockman layer), and one scale height of ionised hydrogen (the Reynolds layer). The vertical size of the domain in the reference model is insufficient to include the scale height of the hot gas, and it would be preferable to consider a computational box of a larger vertical size,  $2L_z$ . Indeed, some similar ISM models use a vertically elongated computational box with the horizontal size of  $1 \text{ kpc} \times 1 \text{ kpc}$  but the top and bottom boundaries at  $L_z = 10 \text{ kpc}$  (e.g., de Avillez & Breitschwerdt 2007, and references therein). However, the horizontal size of the domain  $L_\perp$  in a taller box may need to be increased to keep its aspect ratio of order unity, so as to avoid introducing other unphysical behaviour at  $|z| \gtrsim L_\perp$ .

This constraint arises mainly from the periodic (or sliding periodic) boundary conditions in the horizontal planes as they preclude divergent flows at scales comparable to  $L_\perp$ . However, the scale of the gas flow unavoidably increases with  $|z|$  because of the density stratification. The steady-state continuity equation for a gas stratified in  $z$ ,  $\nabla \cdot \mathbf{u} = -u_z \partial \ln \rho / \partial z$ , leads to the following estimate of the horizontal perturbation velocity arising due to the stratification:

$$u_\perp \simeq u_z \frac{l_\perp}{H}, \quad (8)$$

where  $H$  is the density scale height,  $\partial \ln \rho / \partial z \simeq -H^{-1}$ , and  $l_\perp$  is the horizontal scale of the flow, introduced via  $|\partial u_x / \partial x|, |\partial u_y / \partial y| \simeq u_\perp / l_\perp$ . Here we have neglected the vertical variation of  $u_z$ , so that  $\nabla \cdot \mathbf{u} \simeq \partial u_x / \partial x + \partial u_y / \partial y$ : this is justified for the hot and warm gas, since their vertical velocities vary weakly with  $z$  at  $|z| \gtrsim 0.3 \text{ kpc}$  (see Fig. 12). Assuming for the sake of simplicity that  $u_\perp$  is a constant, in Eq. (8), where  $l_{\perp 0}$  is the horizontal correlation length of  $u_\perp$  at  $z = 0$ , we obtain the following estimate of the horizontal correlation length at  $|z| = L_z$ , the top of the domain:

$$l_\perp |_{|z|=L_z} \simeq l_0 + u_\perp t \simeq l_0(1 + L_z/H),$$

where the time available for the expansion is taken as  $t = L_z/u_z$ ,  $l_0$  is the horizontal correlation length of  $u_\perp$  at  $z = 0$ . We find  $l_0 \simeq 0.1 \text{ kpc}$  (Table 5) and  $H \simeq 0.5 \text{ kpc}$  (Fig. 19), so that the correlation scale of the velocity perturbation at the top and bottom boundaries of our domain,  $L_z \approx 1 \text{ kpc}$ , follows as

$$l_\perp |_{|z|=L_z} \simeq 3l_0 \simeq 0.3 \text{ kpc}.$$

Indeed, we find the correlation scale of the random flow increases to 200–300 pc at  $z = 0.8 \text{ kpc}$  (Table 5), so that the diameter of the correlation cell, 400–600 pc becomes comparable to the horizontal size of the domain,  $L_\perp = 1 \text{ kpc}$ . At larger heights, the periodic boundary conditions would suppress the horizontal flows, so that that the continuity equation could only be satisfied via an unphysical increase in the vertical velocity with  $|z|$ . In addition, the size of SN remnants also increases with  $|z|$  as the ambient pressure decreases. Thus, the gas velocity field (and other results) obtained in a model with periodic boundary conditions in  $x$  and  $y$  becomes unreliable at heights significantly exceeding the horizontal size of the computational domain.

The lack of a feedback of the halo on the gas dynamics in the disc can, potentially, affect our results. However, we believe that this is not a serious problem and, anyway, it would not necessarily be resolved by using a taller box of a horizontal size of only 1–2 kpc. The gas flow from the halo is expected to be in the form of

relatively cool, dense clouds, formed at large heights via thermal instability or accreted from the intergalactic space (e.g. Wakker & van Woerden 1997; Putman et al. 2012). A strong direct (as opposed to a long-term) effect of this gas on the multi-phase gas structure in the disc is questionable, as it provides just a fraction of the disc’s star formation rate,  $0.1\text{--}0.2M_{\odot}\text{ yr}^{-1}$  versus  $0.5\text{--}5M_{\odot}\text{ yr}^{-1}$  (Putman et al. 2012). Anyway, a taller computational domain would not help to include the accreted intergalactic gas in simulations of this type. In a galactic fountain, gas returns to the disc at a galactocentric distance at least 3 kpc away from where it starts (Bregman 1980), and this could not be accounted for in models with tall computational boxes that are only 1–2 kpc big horizontally.

In light of these concerns, and since it is not yet possible to expand our domain significantly in all three dimensions, we prefer to restrict ourselves to a box of height  $L_z \approx 1$  kpc, thus retaining an aspect ratio of order unity. This choice of a short box requires great care in the choice of vertical boundary conditions (which might also introduce unphysical behaviour). We discuss our boundary conditions in detail in appendix C, but briefly note here that we use modified open boundary conditions on the velocity at  $z = \pm L_z$ . These conditions allow for both inflow and outflow, and so are to some extent capable of simulating gas exchange between the disc and the halo, driven by processes within the disc. More specifically, matter and energy are free to flow out of and into the computational domain across the top and bottom surfaces if the internal dynamics so require. (An inflow occurs when pressure beneath the surface is lower than at the surface or in the ghost zones).

#### 2.4.2 Numerical resolution

For our standard resolution (numerical grid spacing)  $\Delta x = \Delta y = \Delta z = \Delta = 4$  pc, we use a grid of  $256 \times 256 \times 560$  (excluding ‘ghost’ boundary zones). We apply a sixth-order finite difference scheme for spatial vector operations and a third-order Runge–Kutta scheme for time stepping. We also investigate one model at doubled resolution,  $\Delta = 2$  pc, labelled WSWah in Table 3; the starting state for this model is obtained by remapping a snapshot from the standard-resolution Model WSWa at  $t = 600$  Myr (when the system has settled to a statistical steady state) onto a grid  $512 \times 512 \times 1120$  in size.

Given the statistically homogeneous structure of the ISM in the horizontal directions at the scales of interest (neglecting arm-interarm variations), we apply periodic boundary conditions in the azimuthal ( $y$ ) direction. Differential rotation is modelled using the shearing-sheet approximation with sliding periodic boundary conditions (Wisdom & Tremaine 1988) in  $x$ , the local analogue of cylindrical radius. We apply slightly modified open vertical boundary conditions, described in some detail in Appendix C, to allow for the free movement of gas to the halo without preventing inward flows at the upper and lower boundaries. In the calculations reported here, outflow exceeds inflow on average, and there is a net loss of mass from our domain, of order 15% of the total mass per Gyr. We do not believe that this slow loss of mass significantly affects our results

#### 2.4.3 Transport coefficients

The spatial and temporal resolutions attainable impose lower limits on the kinematic viscosity  $\nu$  and thermal diffusivity  $\chi$ , which are, unavoidably, much higher than any realistic values. These limits result from the Courant–Friedrichs–Lewy (CFL) condition which

requires that the numerical time step must be shorter than the crossing time over the mesh length  $\Delta$  for each of the transport processes involved. It is desirable to avoid unnecessarily high viscosity and thermal diffusivity. The cold and warm phases have relatively small perturbation gas speeds (of order  $10\text{ km s}^{-1}$ ), so we prescribe  $\nu$  and  $\chi$  to be proportional to the local speed of sound,  $\nu = \nu_1 c_s / c_1$  and  $\chi = \chi_1 c_s / c_1$ . We ensure that the maximum Reynolds and Péclet numbers based on the mesh separation  $\Delta$  are always close to unity throughout the computational domain (see Appendix C):  $\nu_1 \approx 4.2 \times 10^{-3}\text{ km s}^{-1}\text{ kpc}$ ,  $\chi_1 \approx 4.1 \times 10^{-4}\text{ km s}^{-1}\text{ kpc}$  and  $c_1 = 1\text{ km s}^{-1}$ . This gives, for example,  $\chi = 0.019\text{ km s}^{-1}\text{ kpc}$  at  $T = 10^5\text{ K}$  and  $0.6\text{ km s}^{-1}\text{ kpc}$  at  $T = 10^8\text{ K}$ . Thus, transport coefficients are larger in the hot gas where typical temperature and perturbation velocity are of order  $10^6\text{ K}$  and  $100\text{ km s}^{-1}$ , respectively. In all models  $\chi \simeq 0.1\nu$ , i.e., the Prandtl number  $\text{Pr} \simeq 10$ . The corresponding fluid Reynolds and Péclet numbers, based on the correlation scale of the flow, fall in the range 20–40 in the models presented here.

Numerical handling of the strong shocks widespread in the ISM needs special care. To ensure that they are always resolved, we include shock-capturing diffusion of heat and momentum, with the diffusivities  $\zeta_\chi$  and  $\zeta_\nu$ , respectively, defined as

$$\zeta_\chi = \begin{cases} c_\chi \Delta x^2 \max_5 |\nabla \cdot \mathbf{u}| & \text{if } \nabla \cdot \mathbf{u} < 0, \\ 0 & \text{otherwise} \end{cases} \quad (9)$$

(and similarly for  $\zeta_\nu$ , but with a coefficient  $c_\nu$ ), where  $\max_5$  denotes the maximum value occurring at any of the five nearest mesh points (in each coordinate). Thus, the shock-capturing diffusivities are proportional to the maximum divergence of the velocity in the local neighbourhood, and are confined to the regions of convergent flow. Here,  $c_\chi = c_\nu$  is a dimensionless coefficient which we have adjusted empirically to 10. This prescription spreads a shock front over sufficiently many (usually, four) grid points. Detailed test simulations of an isolated expanding SN remnant in Appendix B confirm that this prescription produces quite accurate results, particularly those which are relevant to our goals: most importantly, the conversion of thermal to kinetic energy in SN remnants.

With a cooling function susceptible to thermal instability, thermal diffusivity  $\chi$  has to be large enough as to allow us to resolve its most unstable normal modes:

$$\chi \geq \frac{1 - \beta}{\gamma \tau_{\text{cool}}} \left( \frac{\Delta}{2\pi} \right)^2,$$

where  $\beta$  is the cooling function exponent in the thermally unstable range,  $\tau_{\text{cool}}$  is the radiative cooling time and  $\gamma = 5/3$  is the adiabatic index. Figure 4 makes it evident that, in our models,  $\tau_{\text{cool}}$  typically exceeds 1 Myr in the thermally unstable regime. Further details can be found in Appendix D where we demonstrate that, with the parameters chosen in our models, thermal instability is well resolved by the numerical grid.

The shock-capturing diffusion broadens the shocks and increases the spatial spread of density around them. An undesirable effect of this is that the gas inside SN remnants cools faster than it should, thus reducing the maximum temperature and affecting the abundance of the hot phase. Having considered various approaches while modelling individual SN remnants in Appendix B, we adopt a prescription which is numerically stable, reduces gas cooling within SN remnants, and confines extreme cooling to the shock fronts. Specifically, we multiply the term  $(\Gamma - \rho\Lambda)T^{-1}$  in Eq. (3) by

$$\xi = \exp(-C|\nabla\zeta_\chi|^2), \quad (10)$$

**Table 3.** Selected parameters of the numerical models explored in this paper, named in Column (1). Columns (2)–(3) give input parameters: numerical resolution  $\Delta$  and initial mid-plane gas number density  $n_0$ . The remaining columns give output parameters: (4) time span over which the models have been in steady state (in the units of  $\tau = L_x/u_{0,\text{rms}}$ , the typical horizontal crossing time based on the root-mean-square (r.m.s.) random speed  $u_0$  given in Column (9) and  $L_x \approx 1$  kpc); (5) average kinematic viscosity  $\langle \nu \rangle$ ; (6) average sound speed  $\langle c_s \rangle$ ; (7)–(8) average Reynolds numbers defined at the grid spacing,  $\Delta$ , and based on the correlation scale of the random flow,  $l_0 \simeq 100$  pc; (9)–(10) r.m.s. perturbation velocity  $u_{\text{rms}}$ , and r.m.s. random velocity  $u_{0,\text{rms}}$ ; (11) thermal energy density  $e_{\text{th}}$ ; (12) kinetic energy density  $e_{\text{kin}}$ ; and (13) volume fractions  $f_V$  of cold (C), warm (W) and hot (H) gas at  $|z| \leq 200$  pc.

(1)	(2)	(3)	(4)	(5)	(6)	(7)	(8)	(9)	(10)	(11)	(12)	(13)
Model	$\Delta$ [pc]	$n_0$ [ $\frac{1}{\text{cm}^3}$ ]	$\Delta t$ [ $\tau$ ]	$\langle \nu \rangle$ [ $\frac{\text{km kpc}}{\text{s}}$ ]	$\langle c_s \rangle$ [ $\text{km s}^{-1}$ ]	$\langle \text{Re}_\Delta \rangle$	$\langle \text{Re} \rangle$	$u_{\text{rms}}$ [ $\text{km s}^{-1}$ ]	$u_{0,\text{rms}}$ [ $\text{km s}^{-1}$ ]	$e_{\text{th}}$ [ $\frac{E_{\text{SN}}}{\text{kpc}^3}$ ]	$e_{\text{kin}}$ [ $\frac{E_{\text{SN}}}{\text{kpc}^3}$ ]	$f_V$ , C:W:H [%]
WSWa	4	1.8	3.9	0.44	108	0.88	22	76	26	30	13	2 : 60 : 38
WSWah	2	1.8	0.5	0.77	186	0.85	43	103	34	19	10	3 : 51 : 46
RBN	4	2.1	2.7	0.24	58	1.18	30	37	18	25	9	3 : 82 : 15
WSWb	4	2.1	4.0	0.27	65	0.97	24	45	20	29	13	3 : 70 : 27

where  $\zeta_\chi$  is the shock diffusivity defined in Eq. (9). Thus,  $\xi \approx 1$  almost anywhere in the domain but reduces towards zero in strong shocks, where  $|\nabla \zeta_\chi|^2$  is large. The value of the additional empirical parameter,  $C \approx 0.01$ , was chosen to ensure numerical stability with minimum change to the basic physics. We have verified that, acting together with other artificial diffusion terms, this does not prevent accurate modelling of individual SN remnants (see Appendix B).

#### 2.4.4 Initial conditions

We adopt an initial density distribution corresponding to *isothermal* hydrostatic equilibrium in the gravity field of Eq. (7):

$$\rho(z) = \rho_0 \exp \left[ a_1 \left( z_1 - \sqrt{z_1^2 + z^2} - \frac{a_2}{2a_1} \frac{z^2}{z_2} \right) \right]. \quad (11)$$

Since our present model does not contain magnetic fields or cosmic rays, which provide roughly half of the total pressure in the ISM (the remainder coming from thermal and turbulent pressures), we expect the gas scale height to be smaller than that observed. Given the limited spatial resolution of our simulations, the correspondingly weakened thermal instability and neglected self-gravity, it is not quite clear in advance whether the gas density used in our model should include molecular hydrogen or, alternatively, include only diffuse gas.

We used  $\rho_0 = 3.5 \times 10^{-24} \text{ g cm}^{-3}$  for models RBN and WSWb, corresponding to gas number density,  $n_0 = 2.1 \text{ cm}^{-3}$  at the mid-plane. This is the total interstellar gas density, including the part confined to molecular clouds. These models, discussed in Section 8.2, exhibit unrealistically strong cooling. Therefore, the subsequent models WSWa and WSWah have a smaller amount of matter in the computational domain (a 17% reduction), with  $\rho_0 = 3.0 \times 10^{-24} \text{ g cm}^{-3}$ , or  $n_0 = 1.8 \text{ cm}^{-3}$ , accounting only for the atomic gas (see also Joung & Mac Low 2006).

As soon as the simulation starts, density-dependent heating and cooling affect the gas temperature, so it is no longer isothermal and  $\rho(z)$  given in Eq. (11) is not a hydrostatic distribution. To avoid unnecessarily long initial transients, we impose a non-uniform initial temperature distribution so as to be near static equilibrium:

$$T(z) = \frac{T_0}{z_1} \left( \sqrt{z_1^2 + z^2} + \frac{a_2}{2a_1} \frac{z^2}{z_2} \right), \quad (12)$$

where  $T_0$  is obtained from

$$\Gamma(0) = \rho_0 \Lambda(T_0) \approx 0.0147 \text{ erg g}^{-1} \text{ s}^{-1}.$$

The value of  $T_0$  therefore depends on  $\rho_0$  and the choice of the cooling function.

## 2.5 Models explored

We considered four numerical models, with relevant input parameters listed in Table 3, along with some output parameters describing the results. The models are labelled with prefix RBN or WSW according to the cooling function used. Angular brackets in Table 3 denote averages over the whole volume, taken from eleven snapshots (10 for WSWah) within the statistical steady state. The time span,  $\Delta t$ , is given in Column 4, normalised by  $\tau = L_x/u_{0,\text{rms}}$ , where  $u_{0,\text{rms}}$  is the root-mean-square random velocity and  $L_x \approx 1$  kpc is the horizontal size of the computational domain (e.g.,  $\tau \approx 38$  Myr in Model WSWa). As  $\nu$  is set proportional to the speed of sound  $c_s$ , it is variable and the table presents its average value  $\langle \nu \rangle = \nu_1 \langle c_s \rangle / c_1$ , where  $\nu_1 = 0.004 \text{ km s}^{-1} \text{ kpc}$  and  $c_1 = 1 \text{ km s}^{-1}$  in all models. The numerical resolution is adequate when the mesh Reynolds number,  $\text{Re}_\Delta = u \Delta / \nu$ , does not exceed a certain value (typically between 1 and 10) anywhere in the domain, where  $\Delta$  is the grid spacing (4 pc for all models, except for Model WSWah, where  $\Delta = 2$  pc). Therefore, we ensure that  $u_{\text{max}} \Delta / \nu < 5$ , where  $u_{\text{max}}$  is the maximum perturbation velocity at any time and any grid point. The indicative values in Table 3 are averages of the mesh Reynolds number,  $\langle \text{Re}_\Delta \rangle = \langle u_0 / c_s \rangle \Delta c_1 / \nu_1$ , and the Reynolds number,  $\langle \text{Re} \rangle = \langle u_0 / c_s \rangle l_0 c_1 / \nu_1$ . The Reynolds number based on the correlation scale of the random flow,  $l_0 \simeq 100$  pc, is thus 25 times larger than  $\text{Re}_\Delta$  in all models explored here except for Model WSWah, where the difference is a factor of 50.

The quantities shown in Table 3 have been calculated as follows. In Column 9, the r.m.s. perturbation velocity  $u_{\text{rms}}$  is derived from the total perturbation velocity field  $\mathbf{u}$ , which excludes only the overall galactic rotation  $\mathbf{U}$ . In Column 10, the r.m.s. random velocity  $u_{0,\text{rms}}$  is obtained with the mean flows  $\langle \mathbf{u} \rangle_\ell$ , defined in Eq. (6), deducted from  $\mathbf{u}$ . In Columns 11 and 12,  $e_{\text{th}} = \langle \rho e \rangle$  and  $e_{\text{kin}} = \langle \frac{1}{2} \rho u^2 \rangle$  are the average thermal and kinetic energy densities, respectively; the latter includes the perturbation velocity  $\mathbf{u}$  and both are normalised to the SN energy  $E_{\text{SN}}$ . The values of the volume fractions of the cold, warm and hot phases (defined in Section 4) near the mid-plane are given in Column 13.

The reference model, WSWa, uses the WSW cooling function but with lower gas density than WSWb, to exclude molecular hydrogen (see Section 3). Model WSWah, which differs from WSWa only in its spatial resolution, is designed to clarify the effects of

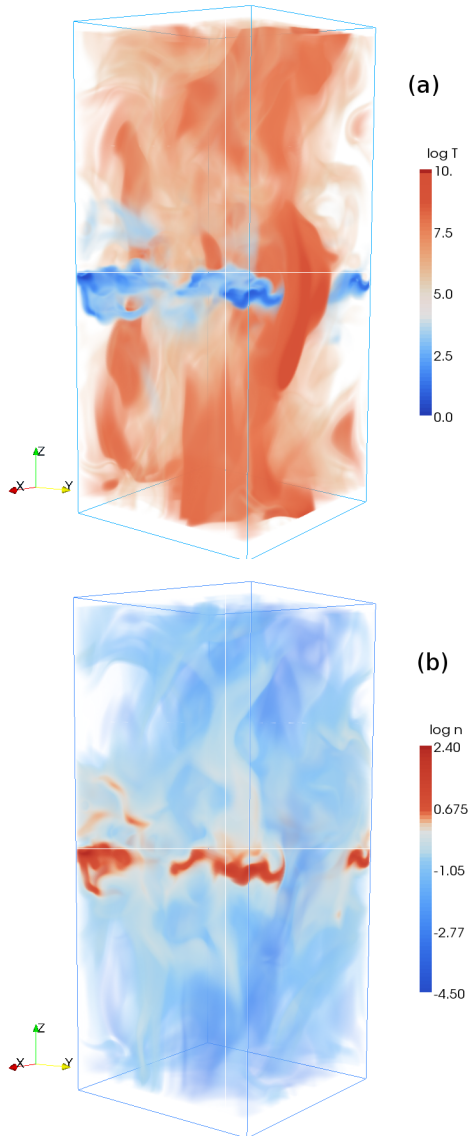


**Figure 2.** A 3D rendering of (a) temperature  $T$  and (b) density  $n$  in Model WSWa at  $t = 551$  Myr. Cold, dense gas is mostly restricted near the mid-plane, whereas hot gas extends towards the boundaries. To aid visualisation of 3D structure, warm gas ( $10^3 < T < 10^6$  K) in the panel (a) and diffuse ( $n < 10^{-2} \text{ cm}^{-3}$ ) in panel (b) have high transparency. Thus the extreme temperatures or dense structures are emphasised.

resolution on the results. We also analyze two models which differ only in the cooling function, RBN and WSWb, to assess the sensitivity of the results to this choice.

### 3 THE REFERENCE MODEL

Model WSWa is taken as a reference model; it has rotation corresponding to a flat rotation curve with the Solar angular velocity, and gas density reduced to exclude that part which would have entered molecular clouds. Results for this model were obtained by the continuation of the Model WSWb, in which the mass from molecular hydrogen had been included: at  $t \approx 400$  Myr, the mass of gas in the domain was changed to that of Model WSWa by reducing gas

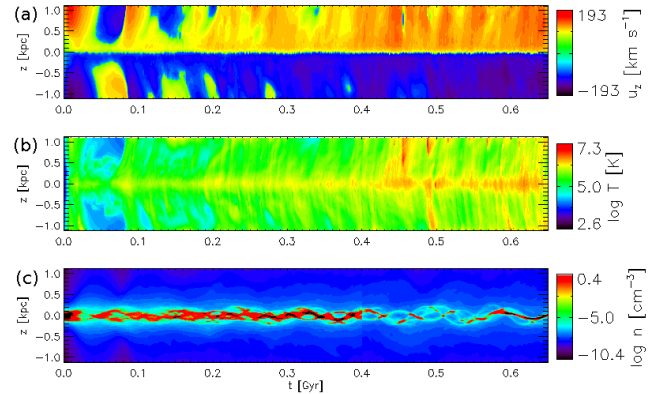


**Figure 3.** Horizontal ( $xy$ ) averages of (a) the vertical velocity, (b) temperature and (c) gas density as functions of time for Model WSWa (Model WSWb up to 0.4 Gyr).

density by 15% at every mesh point. The effect of this change of the total mass is discussed in Section 8.2.

Figure 2 shows typical temperature and density distributions in this model at  $t = 551$  Myr (i.e., 151 Myr after the restart from Model WSWb with reduced density). Supernova remnants appear as irregularly shaped regions of hot, dilute gas. A hot bubble breaking through the cold gas layer extends from the mid-plane towards the lower boundary, visible as a vertically stretched region in the temperature snapshot near the ( $x, z$ )-face. Another, smaller one can be seen below the mid-plane near the ( $y, z$ )-face. Cold, dense structures are restricted to the mid-plane and occupy a small part of the volume. Very hot and cold regions exist in close proximity.

Horizontally averaged quantities are shown in Fig. 3 as functions of  $z$  and time for Model WSWb at  $t < 400$  Myr, and WSWa at later times, showing the effect of reducing the total mass of gas at the transition time. Average quantities may have limited physical significance because the multi-phase gas has an extremely wide range of velocities, temperatures and densities. For example, panel (b) shows that the average temperature near the mid-plane,  $|z| \lesssim 0.35$  pc, is, perhaps unexpectedly, generally higher than that at the larger heights. This is due to Type II SN remnants, which contain very hot gas with  $T \gtrsim 10^8$  K and are concentrated near the mid-plane; even though their total volume is small, they significantly affect the average temperature.

Nevertheless these help to illustrate some global properties of the multi-phase structure. Before the system settles into a quasi-stationary state at about  $t = 250$  Myr, it undergoes a few large-scale transient oscillations involving quasi-periodic vertical motions. The period of approximately 100 Myr, is consistent with the breathing modes identified by Walters & Cox (2001) and attributed to oscillations in the gravity field. Gas falling from high altitude overshoots the midplane and thus oscillates around it. Turbulent and molecular viscosities dampen these modes. At later times, a systematic outflow develops with an average speed of about  $100 \text{ km s}^{-1}$ ; we note that the vertical velocity increases very rapidly near the mid-plane and varies much less at larger heights. The result of the reduction of gas density at  $t \approx 400$  Myr is clearly visible, as it leads to higher mean temperatures and a stronger and more regular outflow, together with a less pronounced and more disturbed layer of cold gas.

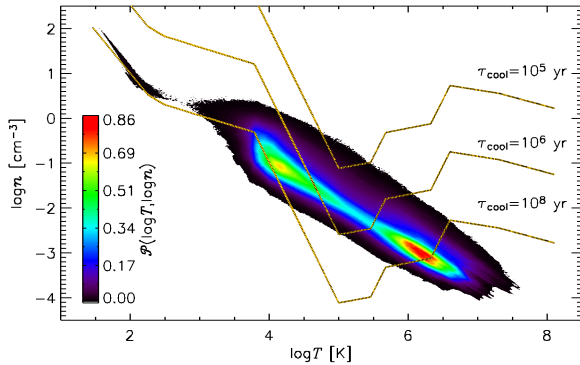


**Figure 4.** The joint probability density of the gas number density and temperature, shown for the whole computational domain using 11 snapshots of Model WSWa in a statistically steady state for  $634 \leq t \leq 644$  Myr. Contours of constant cooling time  $\tau_{\text{cool}} = 10^5$ ,  $10^6$  and  $10^8$  yr, are shown to clarify the importance of radiative cooling in the model.

#### 4 THE MULTI-PHASE STRUCTURE

All models discussed here have a well-developed multi-phase structure apparently similar to that observed in the ISM. Since the ISM phases are not genuine, thermodynamically distinct phases (e.g. Vázquez-Semadeni 2012), their definition is tentative, with the typical temperatures of the cold, warm and hot phases usually adopted as  $T \simeq 10^2$  K,  $10^4$ – $10^5$  K and  $10^6$  K, respectively. However, the borderline temperatures (and even the number of distinct phases) can be model-dependent, and they are preferably determined by considering the results, rather than *a priori*. Inspection of the probability distribution of gas number density and temperature, displayed in Fig. 4, reveals three distinct concentrations at  $(T[\text{K}], n[\text{cm}^{-3}]) = (10^2, 10)$ ,  $(10^4, 10^{-1})$  and  $(10^6, 10^{-3})$ . Thus, we can confirm that the gas structure in this model can be reasonably well described in terms of three distinct phases. Moreover, we can identify the boundaries between them as the temperatures corresponding to the minima of the joint probability distribution at about 500 K and  $5 \times 10^5$  K.

The curves of constant cooling time, also shown in Fig. 4, suggest that the distinction between the warm and hot gas is due to the maximum of the cooling rate near  $T = 10^5$  K (see also Fig. 1), whereas the cold, dense gas, mainly formed by compression (see below), closely follows the curve  $\tau_{\text{cool}} \approx 10^8$  yr.

In Fig. 5, we show the probability distributions of gas number density, random velocity, Mach number, thermal and total pressures within each phase in Model WSWa. The overlap in the gas density distributions (Fig. 5a) is small (at the probability densities of order  $\mathcal{P} = 0.1$ ). The ratios of the probability densities near the maximum for each phase (mode) are about 100; the modal densities,  $n \approx 10^{-3}$ ,  $10^{-1}$  and  $10 \text{ cm}^{-3}$ , thus typify the hot, warm and cold gas respectively.

The velocity probability distributions in Fig 5b reveal a clear connection between the magnitude of the random velocity of gas and its temperature: the r.m.s. velocity in each phase scales with its speed of sound. This is confirmed by the Mach number distributions in Fig. 5c: both warm and hot phases are transonic with respect to their sound speeds. The cold gas is mostly supersonic, having speeds typically under  $10 \text{ km s}^{-1}$ . The double peak in the probability density for the cold gas velocity (Fig 5b) (and the corresponding extension of the Mach number distribution to  $\mathcal{M} \gtrsim 1$ ) is a robust feature, not dependent on the temperature boundary of the

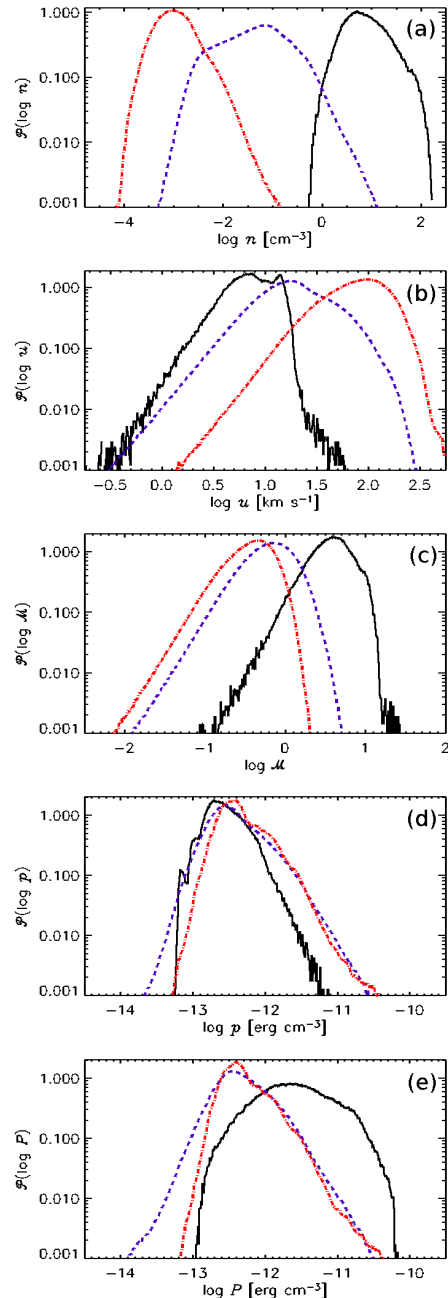


**Figure 5.** The probability distributions of (a) density, (b) random velocity,  $u_0$  (c) Mach number of random motions  $u_0$  (defined with respect to the local speed of sound), (d) thermal pressure, and (e) total pressure, for each phase of Model WSWa, using 11 snapshots spanning  $t = 634$  to  $644$  Myr and presented for each phase: cold  $T < 500$  K (black, solid line), warm  $500 \leq T < 5 \times 10^5$  K (blue, dashed), and hot  $T \geq 5 \times 10^5$  K (red, dash-dotted).

cold gas. This plausibly includes ballistic gas motion in the shells of SN remnants, as well as bulk motions of cold clouds at subsonic or transonic speed with respect to the ambient warm gas.

Probability densities of thermal pressure, shown in Fig. 5d, are notable for the relatively narrow spread: one order of magnitude, compared to a spread of six orders of magnitude in gas density. Moreover, the three phases have overlapping thermal pressure distributions, suggesting that the system is in a statistical ther-

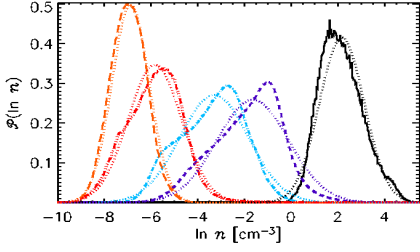


**Figure 6.** The probability distributions of gas density in model WSWa for the cold (black, solid), warm and hot gas. The warm/hot gas have been divided into regions  $|z| \leq 200$  pc (purple/red, dashed/dash-triple-dotted) and  $|z| > 200$  pc (light blue/orange, dash-dotted/long-dashed). The best-fit lognormal distributions are shown dotted in matching colour.

**Table 4.** Parameters of the lognormal fits to the distribution of gas number density  $n$  in various phases, where  $\mu_n$  and  $s_n$  are defined in Eq. (13).

Phase	$\mu_n$ [ln cm $^{-3}$ ]	$s_n$ [ln cm $^{-3}$ ]
cold	2.02	0.92
warm ( $ z  \leq 200$ pc)	-1.64	1.47
warm ( $ z  > 200$ pc)	-3.29	1.47
warm (total)	-3.03	1.47
hot ( $ z  \leq 200$ pc)	-5.78	1.20
hot ( $ z  > 200$ pc)	-6.96	0.77

mal pressure balance. However, thermal pressure is not the only part of the total pressure in the gas, which here includes the turbulent pressure  $\frac{1}{3}\rho\langle\mathbf{u} - \langle\mathbf{u}\rangle_\ell\rangle^2$ , where  $\langle\mathbf{u}\rangle_\ell$ , defined in Eq. (6), is the mean fluctuation velocity. As shown in Fig. 13, total kinetic energy within the computational domain, associated with random flows, is about a third of the thermal pressure. Correspondingly, the total pressure distributions in Fig. 5e peaks at about  $4 \times 10^{-13}$  dyn cm $^{-2}$  (or erg cm $^{-3}$ ), for both the warm and hot gas. The cold gas appears somewhat overpressured, with the modal pressure at  $2 \times 10^{-12}$  dyn cm $^{-2}$ , and with some regions under pressure as high as  $10^{-11}$  dyn cm $^{-2}$ . It becomes apparent (see the discussion of Fig 7, below) that this is due to both compression by transonic random flows and the vertical pressure gradient. All the cold gas occupies the higher pressure mid-plane, while the warm and hot gas distributions mainly include lower pressure regions away from the disc.

Cold, dense clouds are formed through radiative cooling facilitated by compression, which has more importance than in the other, hotter phases. The compression is, however, truncated at the grid scale of 4 pc, preventing the emergence of higher densities in excess of about  $10^2$  cm $^{-3}$ .

The probability distributions of gas density in Fig. 5a can be reasonably approximated by the lognormal distributions, of the form

$$\mathcal{P}(n) = \Lambda(\mu_n, s_n) \equiv \frac{1}{ns_n\sqrt{2\pi}} \exp\left(-\frac{(\ln n - \mu_n)^2}{2s_n^2}\right). \quad (13)$$

The quality of the fits is illustrated in Fig. 6, using 500 data bins in the range  $10^{-4.8} < n < 10^{2.5}$  cm $^{-3}$ ; the best-fit parameters are given in Table 4. Note that, in making these fits, we have subdivided the hot and warm gas into that near the mid-plane ( $|z| \leq 200$  pc) and that at greater heights ( $|z| > 200$  pc); the former is located in the SN active region, strongly shocked with a broad range of density and pressure fluctuations, whereas the latter is predominantly

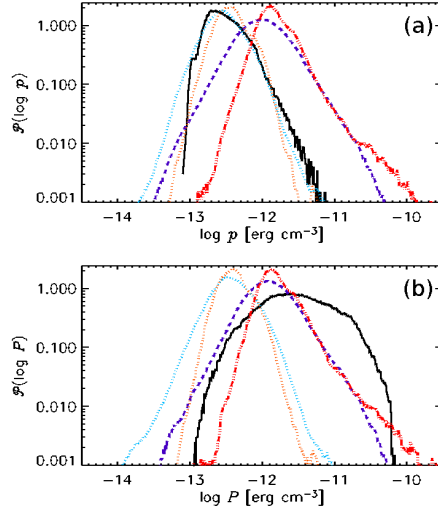


**Figure 7.** Probability distributions for (a) thermal pressure  $p$  and (b) total pressure  $P$  in Model WSWa, for different gas phases: cold (black, solid); warm (blue, dashed) and hot (red, dash-triple-dotted) at  $|z| \leq 200$  pc; warm (light blue, dotted) and hot (orange, dotted) at  $|z| > 200$  pc.

the more diffuse and homogeneous gas in the halo. As can be seen in Fig. 6, the shape of the probability distribution of the warm gas (rather than the position of its maximum) does not vary much with  $|z|$ . Table 4, thus shows the parameters for the warm in the whole volume. The lognormal fits satisfy the Kolmogorov-Smirnov test at or above the 95% level of significance. For the hot gas fit the KS test fails for the total volume. So only the fits for the hot gas split by height are included in Table 4.

The probability densities of thermal and total pressure, displayed in Fig. 7, show that although the thermal pressure of the cold gas near the mid-plane is lower than in the other phases the total pressures are much closer to balance. The broad probability distribution of the cold gas density is consistent with multiple compressions in shocks. The hot and warm gas pressure distributions are also approximately lognormal. The gas at  $|z| > 200$  pc (dotted lines) appears to be in both thermal and total pressure balance.

In summary, we conclude that the system is close to the state of statistical pressure equilibrium: the total pressure has similar values and similar probability distributions in each phase. Jounge et al. (2009) also conclude from their simulations that the gas is in both thermal and total pressure balance. This could be expected, since the only significant deviation from the statistical dynamic equilibrium of the system is the vertical outflow of the hot gas and entrained warm clouds (see Section 7).

## 5 THE FILLING FACTOR AND FRACTIONAL VOLUME

### 5.1 Filling factors: basic ideas

The *fractional volume* of the ISM occupied by the phase  $i$  is given by

$$f_{V,i} = \frac{V_i}{V} \quad (14)$$

where  $V_i$  is the volume occupied by gas in the temperature range defining phase  $i$  and  $V$  is the total volume. How the gas is distributed *within* a particular phase is described by the *phase filling*

factor

$$\phi_i = \frac{\overline{n_i}^{-2}}{n_i^2}, \quad (15)$$

where the over bar denotes a *phase average*, i.e., an average only taken over the volume occupied by the phase  $i$ .  $\phi_i$  describes whether the gas density of a phase is homogeneous ( $\phi_i = 1$ ) or clumpy ( $\phi_i < 1$ ). Both of these quantities are clearly important parameters of the ISM, allowing one to characterise, as a function of position, both the relative distribution of the phases and their internal structure. As discussed below, the phase filling factor is also directly related to the idea of an ensemble average, an important concept in the theory of random functions and so  $\phi_i$  provides a useful connection between turbulence theory and the astrophysics of the ISM. Both  $f_{V,i}$  and  $\phi_i$  are easy to calculate in a simulated ISM by simply counting mesh-points.

In the real ISM, however, neither  $f_V$  nor  $\phi_i$  can be directly measured. Instead the *volume filling factor* can be derived (Reynolds 1977; Kulkarni & Heiles 1988; Reynolds 1991),

$$\Phi_i = \frac{\langle n_i \rangle^2}{\langle n_i^2 \rangle}, \quad (16)$$

for a given phase  $i$ , where the angular brackets denote a *volume average*, i.e., taken over the total volume.<sup>2</sup>

Most work in this area to-date has concentrated on the diffuse ionised gas (or warm ionised medium) since the emission measure of the free electrons  $EM \propto n_e^2$  and the dispersion measure of pulsars  $DM \propto n_e$ , allowing  $\Phi$  to be estimated along many lines-of-sight (e.g. Reynolds 1977; Kulkarni & Heiles 1988; Reynolds 1991; Berkhuijsen et al. 2006; Hill et al. 2008; Gaensler et al. 2008). It is useful to generalise the tools derived to interpret the properties of a *single* ISM phase for the case of the *multiphase* ISM, as this can help to avoid potential pitfalls when combining data from different sources with similar-sounding names (filling factor, filling fraction, fractional volume, etc.) but subtly different meanings. In particular, only under the very specific conditions explained below, do the volume filling factors  $\Phi_i$  of the different phases of the ISM sum to unity.

In terms of the volume  $V_i$  occupied by phase  $i$ ,

$$\overline{n_i} = \frac{1}{V_i} \int_{V_i} n_i dV, \quad (17)$$

whilst

$$\langle n_i \rangle = \frac{1}{V} \int_V n_i dV = \frac{1}{V} \int_{V_i} n_i dV, \quad (18)$$

the final equality holding because  $n_i = 0$  outside the volume  $V_i$  by definition. Since the two types of averages differ only in the volume over which they are averaged, they are related by the fractional volume:

$$\langle n_i \rangle = \frac{V_i}{V} \overline{n_i} = f_{V,i} \overline{n_i}, \quad (19)$$

and

$$\langle n_i^2 \rangle = \frac{V_i}{V} \overline{n_i^2} = f_{V,i} \overline{n_i^2}. \quad (20)$$

<sup>2</sup> As with the density filling factors introduced here, filling factors of temperature and other variables can be defined similarly to Eqs. (15) and (16), for example  $\phi_{T,i} = \overline{T_i}^{-2}/T_i^2$ , etc.

Consequently, the *volume filling factor*  $\Phi_{n,i}$  and the *phase filling factor*  $\phi_{n,i}$  are similarly related:

$$\Phi_i = \frac{\langle n_i \rangle^2}{\langle n_i^2 \rangle} = f_{V,i} \frac{\overline{n_i}^2}{n_i^2} = f_{V,i} \phi_i. \quad (21)$$

Thus the parameters of most interest,  $f_{V,i}$  and  $\phi_{n,i}$ , characterizing the fractional volume and the degree of homogeneity of a phase respectively, are related to the observable quantity  $\Phi_{n,i}$  by Eq. (21). This relation is only straightforward when the ISM phase can be assumed to be homogeneous or if one has additional statistical knowledge, such as the probability density function, of the phase. In the next sub-section we use two simple examples to illustrate how the ideas developed here can be applied to the real ISM; we then use them to develop a new interpretation of existing observational data and finally discuss how the properties of our simulated ISM compare to observations. But first a brief note about different methods of averaging is necessary.

### 5.1.1 Averaging methods for observations and theory

An important feature of the definition of the volume filling factor given by Eq. (15), is that the averaging involved is inconsistent with that used in theory of random functions. In the latter, the calculation of volume (or time) averages is usually complicated or impossible and, instead, ensemble averages (i.e. averages over the relevant probability distribution functions) are used; the ergodicity of the random functions is relied upon to ensure that the two averages are identical to each other (Section 3.3 in Monin & Yaglom 2007; Tennekes & Lumley 1972). But the volume filling factors  $\Phi_i$  are not compatible with such a comparison, as they are based on averaging over the total volume, despite the fact that each phase occupies only a fraction of it. In contrast, the phase averaging used to derive  $\phi_i$  is performed only over the volume of each phase, and so should correspond better to results from the theory of random functions.

## 5.2 Filling factors: applications

### 5.2.1 Assumption of homogeneous phases

The simplest way to interpret an observation of the volume filling factor  $\Phi_i$  is to assume that each ISM phase has a constant density. Consider Eqs. (14), (15) and (16) for an idealised two-phase system, where each phase is homogeneous. (These arguments can easily be generalised to an arbitrary number of homogeneous phases.) For example a set of discrete clouds of one phase, of constant density and temperature, embedded within the other phase, with different (but also constant) density and temperature. Let one phase have (constant) gas number density  $N_1$  and occupy volume  $V_1$ , and the other  $N_2$  and  $V_2$ , respectively. The total volume of the system is  $V = V_1 + V_2$ .

The volume-averaged density of each phase, as required for Eq. (16), is given by

$$\langle n_i \rangle = \frac{N_i V_i}{V} = f_{V,i} N_i. \quad (22)$$

where  $i = 1, 2$ . Similarly, the volume average of the squared density is

$$\langle n_i^2 \rangle = \frac{N_i^2 V_i}{V} = f_{V,i} N_i^2. \quad (23)$$

The fractional volume of each phase can then be written as

$$f_{V,i} = \frac{\langle n_i \rangle^2}{\langle n_i^2 \rangle} = \frac{\langle n_i \rangle}{N_i} = \Phi_i, \quad (24)$$

with  $f_{V,1} + f_{V,2} = 1$ , and  $\Phi_1 + \Phi_2 = 1$ . The volume-averaged quantities satisfy  $\langle n \rangle = \langle n_1 \rangle + \langle n_2 \rangle = f_{V,1}N_1 + f_{V,2}N_2$  and  $\langle n^2 \rangle = \langle n_1^2 \rangle + \langle n_2^2 \rangle = f_{V,1}N_1^2 + f_{V,2}N_2^2$ , with the density variance  $\sigma^2 \equiv \langle n^2 \rangle - \langle n \rangle^2 = f_{V,1}f_{V,2}(N_1 - N_2)^2$ .

In contrast, the phase-averaged density of each phase, used to calculate the phase filling factor Eq. (15), is simply  $\bar{n}_i = N_i$ , and the phase average of the squared density is  $\bar{n}_i^2 = N_i^2$ , so that the phase filling factor is  $\phi_i = 1$ , as must be the case for a homogeneous phase.

Thus for homogeneous phases, the volume filling factor and the fractional volume of each phase are identical to each other,  $\Phi_i = f_{V,i}$ , and both sum to unity when considering all phases; in contrast, the phase-averaged filling factor is unity for each phase,  $\phi_i = 1$ . If a given phase occupies the whole volume (i.e., we have a single-phase medium), then all three quantities are simply unity:  $\phi_i = \Phi_i = f_{V,i} = 1$ .

Whilst an assumption of homogeneous phases may be justified for some ISM phases, perhaps in specific regions of the galactic disc, in the case of the simulated ISM discussed in this paper such an assumption would lead to significant underestimates of  $f_{V,i}$  for all phases, by a factor of 2 for the cold and hot gas and by an order of magnitude for the warm gas.

### 5.2.2 Assumption of lognormal phases

For the more realistic case of an inhomogeneous ISM, where each phase consists of gas with a range of densities, the interpretation of  $\Phi_i$  requires additional knowledge about the statistical properties of a phase.

For electrons in the diffuse ionised gas Reynolds (1977) derived the correction factor  $\sigma_c^2/n_c^2$ , where  $n_c$  is the average density of electron clouds and  $\sigma_c^2$  the density variance within clouds, to allow for clumpiness in the electron distribution when calculating the fraction of the total path length occupied by the clouds. More generally, the probability distribution function of the gas in a phase allows  $\phi_i$  to be calculated directly, as we now illustrate for the case of the lognormal PDFs identified in Section 4.

For a lognormal distribution  $\mathcal{P}(n_i) \sim \Lambda(\mu_i, s_i)$ , Eq. (13), the mean and mean-square densities are given by the following phase ('ensemble') averages:

$$\bar{n}_i = e^{\mu_i + s_i^2/2}, \quad \sigma_i^2 = \overline{(n_i - \bar{n}_i)^2} = \bar{n}_i^2 (e^{s_i^2} - 1), \quad (25)$$

where  $\sigma_i^2$  is the density variance around the mean  $\bar{n}_i$ , so that

$$\phi_{n,i} = \frac{\bar{n}_i^2}{\bar{n}_i^2} = \frac{\bar{n}_i^2}{\sigma_i^2 + \bar{n}_i^2} = \exp(-s_i^2). \quad (26)$$

So the phase filling factor  $\phi_{n,i} = 1$  only for a homogeneous density distribution,  $\sigma_i = 0$  (or equivalently,  $s_i = 0$ ). This makes it clear that this filling factor, defined in terms of the phase average, is quite distinct from the fractional volume,  $f_{V,i}$ , but rather quantifies the degree of homogeneity of the gas distribution *within* a given phase. Both describe distinct characteristics of the multi-phase ISM, and, if properly interpreted, can yield rich information about the structure of the ISM.

In the case of the simulated ISM, using the lognormal description of the phases given in Table 4 gives a reasonable agreement between the actual and estimated  $f_{V,i}$  and  $\phi_i$  for all phases, with the biggest discrepancy being an underestimate of  $f_{V,\text{warm}} \approx 0.4$  against a true value of  $f_{V,\text{warm}} \approx 0.6$ .

### 5.2.3 Application to observations

Observations can be used to estimate the volume-averaged filling factor  $\Phi_i$ , defined in Eq. (16), for a given ISM phase. On its own, this quantity is of limited value in understanding how the phases of the ISM are distributed: of more use are the fractional volume occupied by the phase  $f_{V,i}$ , defined in Eq. (14), and its degree of homogeneity which is quantified by  $\phi_i$ , defined by Eq. (15). Knowing  $\Phi_i$  and  $\phi_i$ ,  $f_{V,i}$  follows via Eq. (21):

$$f_{V,i} = \frac{\Phi_{n,i}}{\phi_{n,i}}. \quad (27)$$

This formula is exact, but its applicability in practise is limited if  $\phi_i$  is unknown. However  $\phi_i$  can be deduced from the probability distribution of  $n_i$ : for example if the the density probability distribution of the phase can be approximated by the lognormal, as is expected for a turbulent compressible gas (Vázquez-Semadeni & Garcia 2001; Elmegreen & Scalo 2004), then  $\phi_i$  can be estimated from Eq. (26).

To illustrate how these quantities may be related, let us consider some observations reported for the diffuse ionised gas (the general approach suggested can be applied to any observable or computed quantity). Berkhuijsen et al. (2006) and Berkhuijsen & Müller (2008) estimated  $\Phi_{\text{DIG}}$  for the diffuse ionised gas (DIG) in the Milky Way using dispersion measures of pulsars and emission measure maps. In particular, Berkhuijsen et al. (2006) obtain  $\Phi_{\text{DIG}} \simeq 0.24$  towards  $|z| = 1$  kpc, and Berkhuijsen & Müller (2008) find the smaller value  $\Phi_{\text{DIG}} \simeq 0.08$  for a selection of pulsars that are closer to the Sun than the sample of Berkhuijsen et al. (2006). On the other hand, Berkhuijsen & Fletcher (2008, 2012) used the same data for pulsars with known distances to derive PDFs of the distribution of average DIG cloud densities which are well described by a lognormal distribution; the fitted lognormals have  $s_{\text{DIG}} \simeq 0.32$  (Table 1 in Berkhuijsen & Fletcher 2012). Using Eqs. (26) and (27), this implies that the fractional volume of DIG with allowance for its inhomogeneity is about

$$f_{V,\text{DIG}} \simeq 0.1\text{--}0.3.$$

In other words the combination of  $\Phi_{\text{DIG}}$  and  $s_{\text{DIG}}$  from these results imply that the DIG is approximately homogeneous. This value of  $f_{V,\text{DIG}}$  is in good agreement with the earlier estimates of Reynolds (1977) and Reynolds (1991) who obtained  $f_{V,\text{DIG}} \geq 0.1\text{--}0.2$  and close to that of Hill et al. (2008) who obtained  $f_{V,\text{DIG}} \approx 0.25$  for a vertically stratified ISM, by comparing observed emission and dispersion measures to simulations of isothermal MHD turbulence.

Volume density PDFs derived from observations are still rare. However, PDFs of the column density (and similar observables such as emission measure and dispersion measure) are more easily derived. The applicability of the method outlined in this Section, of deriving the fractional volume occupied by different ISM phases from the (observable) volume filling factor and the PDF of the density distribution, would improve as the relation between the statistical parameters of volume and column density distributions becomes better understood.

### 5.2.4 Simulation results

The filling factors and fractional volumes from Equations (14), (16) and (15) have been computed for the phases identified in Section 4 for the reference model WSWa and presented in Fig. 8. Volumes are considered as discrete horizontal slices. To isolate the  $z$ -

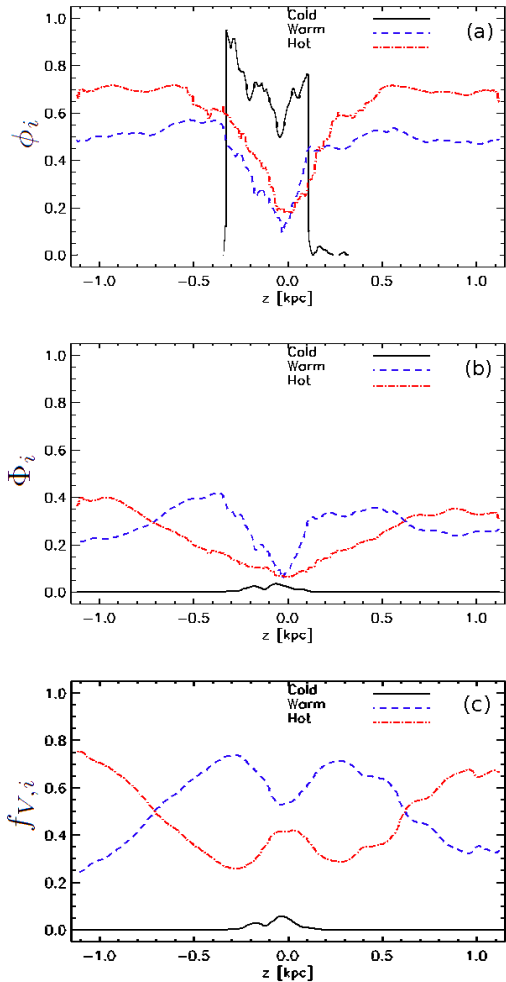


**Figure 8.** Vertical profiles of (a) the phase-averaged density filling factors  $\phi_i = \bar{n}_i^2/n_i^2$  of the gas phases identified in the text: cold (black, solid line,  $T < 500$  K); warm (blue, dashed,  $5 \times 10^2 \leq T < 5 \times 10^5$  K) and hot (red, dash-dotted,  $T \geq 5 \times 10^5$  K); and (b) the volume-averaged density filling factors  $\Phi_i = \langle n_i \rangle^2 / \langle n_i^2 \rangle$ , and (c) the fractional volumes  $f_{V,i}$  with the same line style for each phase. The various filling factors are defined and discussed in Section 5. These results are from 21 snapshots in the interval  $636 \leq t \leq 646$  Myr for Model WSWa.

dependence we averaged over slices of single cell thickness (4 pc-thick).

The hot gas (Fig. 8c) accounts for about 70% of the volume at  $|z| \simeq 1$  kpc and about 40% near the mid-plane. The local maximum of the fractional volume of the hot gas at  $|z| \lesssim 200$  pc is due to the highest concentration of SN remnants there, filled with the very hot gas. Regarding its contribution to integrated gas parameters, it should perhaps be considered as a separate phase.

At  $|z| \lesssim 0.7$  kpc the warm gas accounts for over 50% of the volume. The cold gas occupies a negligible volume, even in the mid-plane where it is concentrated. It is, however, quite homogeneous at low  $|z|$  compared to the warm and hot phases, which only become relatively homogeneous at  $|z| \gtrsim 0.3$  kpc (Fig. 8a).

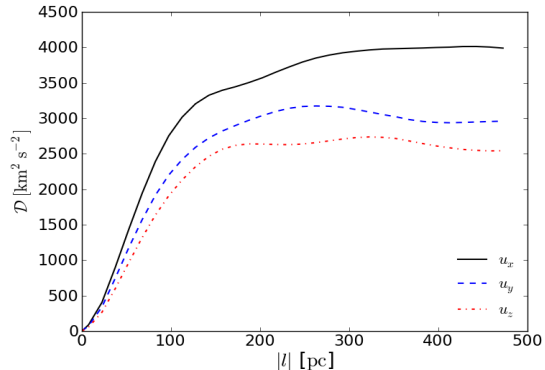


**Figure 9.** The second-order structure functions calculated using Eq. (28), for the layer  $-10 < z < 10$  pc, of the velocity components  $u_x$  (black, solid line),  $u_y$  (blue, dashed) and  $u_z$  (red, dash-dot). The offset  $l$  is confined to the  $(x, y)$ -plane only.

## 6 THE CORRELATION SCALE OF THE RANDOM FLOWS

We have estimated the correlation length of the random velocity  $\mathbf{u}$  at a single time step of the model WSWa, by calculating the second-order structure functions  $\mathcal{D}(l)$  of the velocity components  $u_x$ ,  $u_y$  and  $u_z$ , where

$$\mathcal{D}(l) = \langle [u(\mathbf{x} + \mathbf{l}) - u(\mathbf{x})]^2 \rangle, \quad (28)$$

with  $\mathbf{x}$  the position in the  $(x, y)$ -plane and  $\mathbf{l}$  a horizontal offset. We did not include offsets in the  $z$ -direction and aggregated the squared differences by  $|\mathbf{l}|$  only. Since the flow is expected to be statistically homogeneous horizontally, while the correlation length is expected to vary with  $z$ . A future paper will analyse in more detail the three-dimensional properties of the random flows, including its anisotropy and dependence on height. We measured  $\mathcal{D}(l)$  for five different heights,  $z = 0, 100, -100, 200$  pc and 800 pc, averaging over six adjacent slices in the  $(x, y)$ -plane at each position, corresponding to a layer thickness of 20 pc. The averaging took advantage of the periodic boundaries in  $x$  and  $y$ ; for simplicity we chose a simulation snapshot at a time for which the offset in the  $y$ -boundary, due to the shearing boundary condition, was zero. The structure function for the mid-plane ( $-10 < z < 10$  pc) is shown in Fig. 9.

The correlation scale can be estimated from the form of the structure function since velocities are uncorrelated if  $l$  exceeds the correlation length  $l_0$ , so that  $\mathcal{D}$  becomes independent of  $l$ ,  $\mathcal{D}(l) \approx 2u_{\text{rms}}^2$  for  $l \gg l_0$ . Precisely which value of  $\mathcal{D}(l)$  should be chosen to estimate  $l_0$  in a finite domain is not always clear; for example, the structure function of  $u_y$  in Fig. 9 allows one to make a case for either the value at which  $\mathcal{D}(l)$  is maximum or the value at the greatest  $l$ . Alternatively, and more conveniently, one can estimate  $l_0$  via the autocorrelation function  $\mathcal{C}(l)$ , related to  $\mathcal{D}(l)$  by

$$\mathcal{C}(l) = 1 - \frac{\mathcal{D}(l)}{2u_{\text{rms}}^2}. \quad (29)$$

In terms of the autocorrelation function, the correlation scale  $l_0$  is defined as

$$l_0 = \int_0^\infty \mathcal{C}(l) dl, \quad (30)$$

and this provides a more robust method of deriving  $l_0$  in a finite domain. Of course, the domain must be large enough to make  $\mathcal{C}(l)$

**Table 5.** The correlation scale  $l_0$  and rms velocity  $u_{\text{rms}}$  at various distances from the mid-plane.

$z$	$u_{\text{rms}}$ [km s <sup>-1</sup> ]			$l_0$ [pc]		
	$u_x$	$u_y$	$u_z$	$u_x$	$u_y$	$u_z$
0	45	40	37	99	98	94
100	36	33	43	102	69	124
-100	39	50	46	95	87	171
200	27	20	63	119	105	186
800	51	21	107	320	158	277

negligible at scales of the order of the domain size; this is a non-trivial requirement, since even an exponentially weak tail can make a finite contribution to  $l_0$ . In our estimates we are, of course, limited to the range of  $\mathcal{C}(l)$  within our computational domain, so that the upper limit in the integral of Eq. (30) is equal to  $L_x = L_y$ , the horizontal box size.

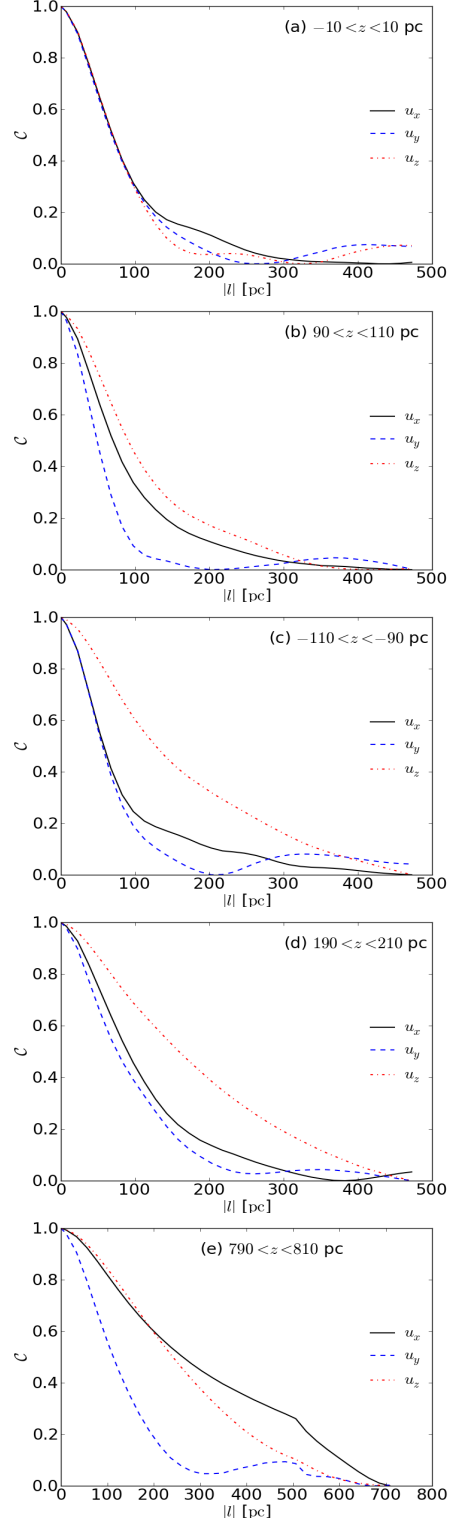
Figure 10 shows  $\mathcal{C}(l)$  for five different heights in the disc, where  $u_{\text{rms}}$  was taken to correspond to the absolute maximum of the structure function,  $u_{\text{rms}}^2 = \frac{1}{2} \max(\mathcal{D})$ , from Eq. (29) at each height.

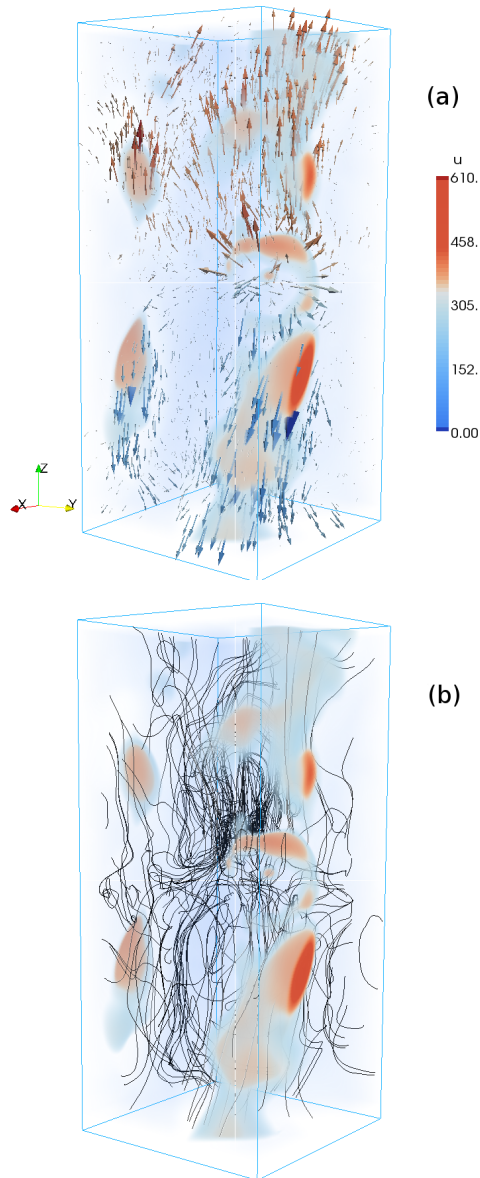
The autocorrelation function of the vertical velocity varies with  $z$  more strongly than, and differently from, the autocorrelation functions of the horizontal velocity components; it broadens as  $|z|$  increases, meaning that the vertical velocity is correlated over progressively greater horizontal distances. Already at  $|z| \approx 200$  pc,  $u_z$  is coherent across a significant horizontal cross-section of the domain, and at  $|z| \approx 800$  pc so is  $u_x$ . An obvious explanation for this behaviour is the expansion of the hot gas streaming away from the mid-plane, which thus occupies a progressively larger part of the volume as it flows towards the halo.

Table 5 shows the rms velocities derived from the structure functions for each component of the velocity at each height, and the correlation lengths obtained from the autocorrelation functions. Note that these are obtained without separation into phases. The uncertainties in  $u_{\text{rms}}$  due to the choices of local maxima in  $\mathcal{D}(l)$  are less than  $2 \text{ km s}^{-1}$ . However, these can produce quite large systematic uncertainties in  $l_0$ , as small changes in  $u_{\text{rms}}$  can lead to  $\mathcal{C}(l)$  becoming negative in some range of  $l$  (i.e. a weak anti-correlation), and this can significantly alter the value of the integral in Eq. (30). Such an anti-correlation at moderate values of  $l$  is natural for incompressible flows; the choice of  $u_{\text{rms}}$  and the estimate of  $l_0$  are thus not straightforward. Other choices of  $u_{\text{rms}}$  in Fig. 9 can lead to a reduction in  $l_0$  by as much as 30 pc. Better statistics, derived from data cubes for a number of different time-steps, will allow for a more thorough exploration of the uncertainties, but we defer this analysis to a later paper.

The rms velocities given in Table 5 are compatible with the global values of  $u_{\text{rms}}$  and  $u_0$  for the reference Model WSWa shown in Table 3. The increase in the rms value of  $u_z$  with height, from about  $40 \text{ km s}^{-1}$  at  $z = 0$  to about  $60 \text{ km s}^{-1}$  at  $z = 200$  pc, reflects the systematic net outflow with a speed increasing with  $|z|$ . There is also an apparent marginal tendency for the rms values of  $u_x$  and  $u_y$  to decrease with increasing distance from the mid-plane.

The correlation scale of the random flow is very close to 100 pc in the mid-plane, and we have adopted this value for  $l_0$  elsewhere in the paper. This estimate is in good agreement with the hydrodynamic ISM simulations of Joung & Mac Low (2006), who found that most kinetic energy is contained by fluctuations with a wavelength (i.e.  $2l_0$  in our notation) of 190 pc. In the MHD simulations of Korpi et al. (1999),  $l_0$  for the warm gas was 30 pc

**Figure 10.** Autocorrelation functions for the velocity components  $u_x$  (black, solid line),  $u_y$  (blue, dashed) and  $u_z$  (red, dash-dot) for 20 pc thick layers centred on four different heights, from top to bottom:  $-10 < z < 10$  pc,  $90 < z < 110$  pc,  $-110 < z < -90$  pc,  $190 < z < 210$  pc and  $790 < z < 810$  pc.



**Figure 11.** The perturbation velocity field  $\mathbf{u}$  in Model WSWa at  $t = 550$  Myr. The colour bar indicates the magnitude of the velocity field depicted in the volume shading, with rapidly moving regions highlighted with shades of red. The low velocity regions, shaded blue, have reduced opacity to assist visualisation. Arrow length of vectors (a) is proportional to the magnitude of  $\mathbf{u}$ , with red (blue) arrows corresponding to  $u_z > 0$  ( $u_z < 0$ ) and independent of the colour bar. Trajectories of fluid elements (b) are also shown, indicating the complexity of the flow and its pronounced vortical structure.

at all heights, but that of the hot gas increased from 20 pc in the mid-plane to 60 pc at  $|z| = 150$  pc. de Avillez & Breitschwerdt (2007) found  $l_0 = 73$  pc on average, with strong fluctuations in time. As in Korpi et al. (1999), there is a weak tendency for  $l_0$  of the horizontal velocity components to increase with  $|z|$  in our simulations, but this tendency remains tentative, and must be examined more carefully to confirm its robustness.

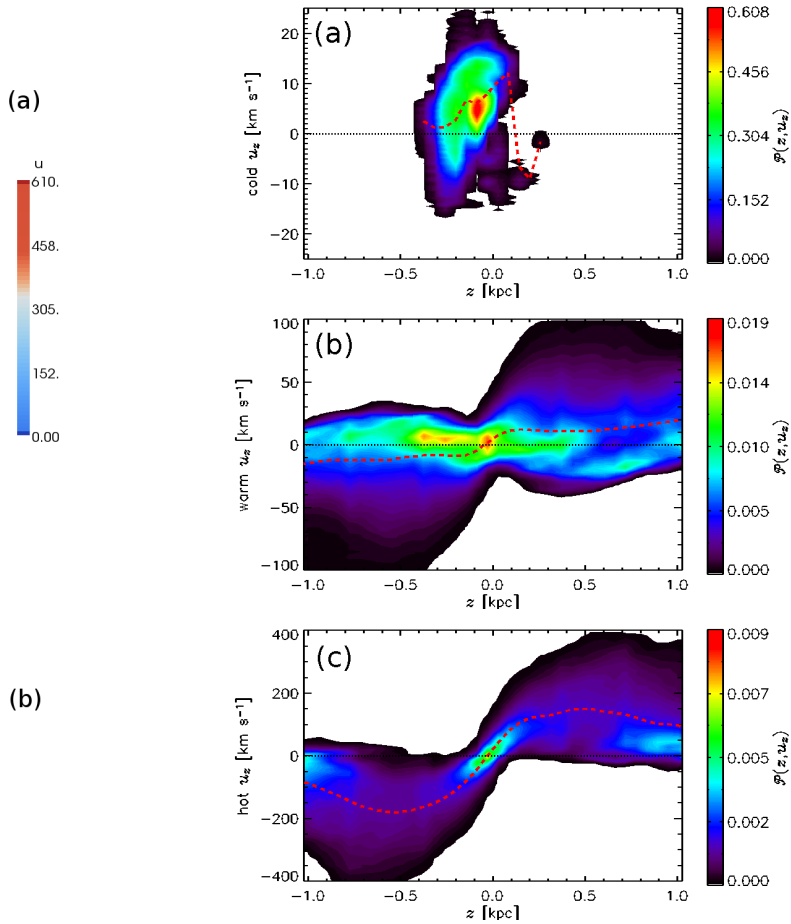


**Figure 12.** Contours of the probability density of the vertical velocity  $u_z$  as a function of  $z$  in Model WSWa from 11 snapshots at  $t = 634$ – $644$  Myr. The cold ( $T < 500$  K), warm ( $500 \text{ K} \leq T < 5 \times 10^5$  K) and hot ( $T \geq 5 \times 10^5$  K) are shown in panels (a) to (c), respectively. The horizontal averages of the vertical velocity  $u_z$  in each case are shown in red, dashed in each panel as well as the mid-plane position (black, dotted).

## 7 GAS FLOW TO AND FROM THE MID-PLANE

Figure 11 illustrates the 3D structure of the perturbation velocity field for the reference Model WSWa. Shades of red show the regions of high speed, whereas regions moving at speeds below about  $300 \text{ km s}^{-1}$  are transparent to aid visualisation. Velocity vectors are shown in panel (a) using arrows, with size indicating the speed, and colour indicating the sign of the  $z$ -component of the velocity (indicating preferential outflow from the mid-plane). Red patches are indicative of recent SN explosions, and there is a strongly divergent flow close to the middle of the  $xz$ -face. In addition, stream lines in panel (b) display the presence of considerable small scale vortical flow near the mid-plane.

The mean vertical flow is dominated by the high velocity hot gas, so it is instructive to consider the velocity structure of each phase separately. Figure 12 shows the probability distributions  $\mathcal{P}(z, u_z)$  as functions of  $u_z$  in the  $(z, u_z)$ -plane from 11 snapshots of Model WSWa, separately for the cold (a), warm (b) and hot gas (c). The cold gas is mainly restricted to  $|z| < 300$  pc and its vertical velocity varies within  $\pm 20 \text{ km s}^{-1}$ . As indicated by the red dashed curve in Panel (a), on average, the cold gas moves towards the mid-plane, presumably after cooling at larger heights. The warm gas

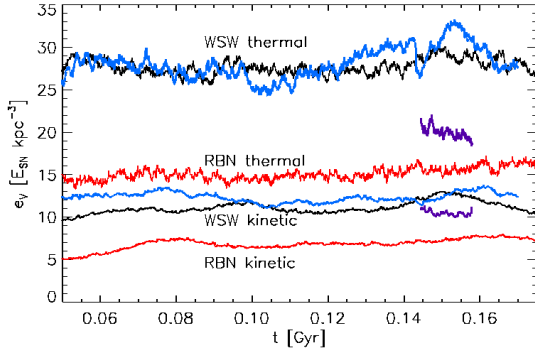


**Figure 13.** Evolution of the volume-averaged thermal energy density (black: model WSWb, blue: model WSWa, purple: model WSWah, red: model RBN) and kinetic energy density (as above; lower lines) in the statistical steady regime, normalised to the SN energy  $E_{\text{SN}} \text{ kpc}^{-3}$ . Models WSWb (black) and RBN (red) essentially differ only in the choice of the radiative cooling function.

is involved in a weak net vertical outflow above  $|z| = 100 \text{ pc}$ , of order  $\pm 10 \text{ km s}^{-1}$ . This might be an entrained flow within the hot gas. However, due to its skewed distribution, the modal flow and thus mass transfer is typically towards the mid-plane. The hot gas has large net outflow speeds, accelerating to about  $100 \text{ km s}^{-1}$  within  $|z| \pm 200 \text{ pc}$ , but with small amounts of inward flowing gas at all heights. The mean hot gas outflow speed increases at an approximately constant rate to somewhat over  $100 \text{ km s}^{-1}$  within  $\pm 100 \text{ pc}$  of the mid-plane, and then decreases with further distance from the mid-plane, at a rate that gradually decreases with height for  $|z| \gtrsim 0.5 \text{ kpc}$ . This is below the escape velocity in the gravitational potential adopted. The structure of the velocity field shall be investigated further elsewhere.

## 8 SENSITIVITY TO MODEL PARAMETERS

### 8.1 The cooling function

We consider two models, RBN and WSWb, with parameters given in Table 3, to assess the effects of the specific choice of the cooling function. Apart from different parameterizations of the radiative cooling, the two models share identical parameters, except the value of  $T_0$  was slightly higher in Model RBN, because of the sensitivity of the initial conditions to the cooling function (Section 2.4.4).

The volume-averaged thermal and kinetic energy densities, the latter excluding the imposed shear flow  $\mathbf{U}$ , are shown in Fig. 13 as functions of time. The averages for each are shown in Columns (11) and (12), respectively of Table 3, using the appropriate steady state time intervals given in Column (4). Models reach a statistical steady-state, with mild fluctuations around a well defined mean value, very soon (within 60 Myr of the start of the simulations). The effect of the cooling function is evident: both the thermal and kinetic energies in Model RBN are about 60% of those in Model WSWb. This is understandable as Model RBN has a stronger cooling rate than Model WSWb, only dropping below the WSW rate in the range  $T < 10^3 \text{ K}$  (see Fig. 1). Interestingly, both models are similar in that the thermal energy is about 2.5 times the kinetic energy.

These results are also remarkably consistent with results by Balsara et al. (2004, their Fig. 6) and Gressel (2008, Fig. 3.1). Gressel (2008) applies WSW cooling and has a model very similar to

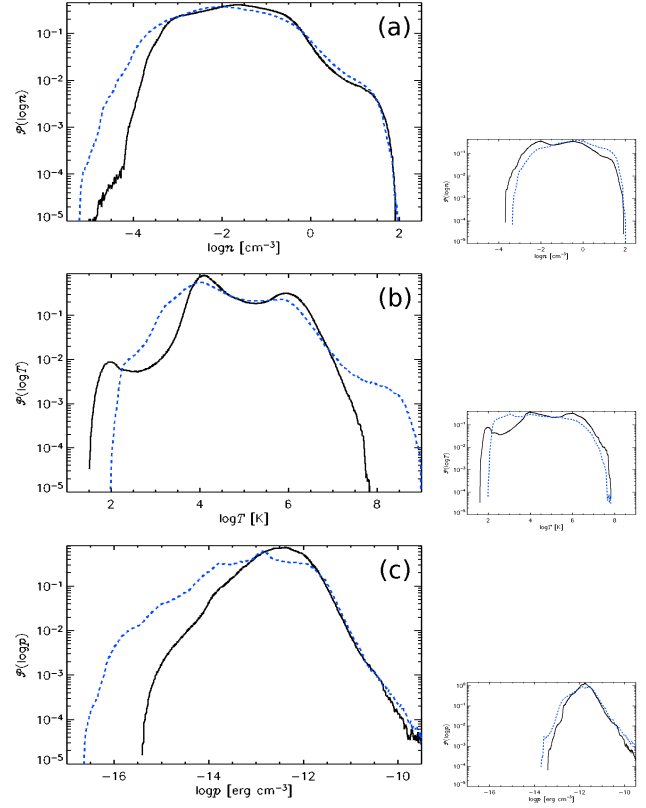


**Figure 14.** Probability density distributions in the whole computational domain, obtained without separation into distinct phases, for (a) gas density, (b) temperature and (c) thermal pressure, for Model RBN (blue, dashed) and Model WSWb (black, solid), in a statistical steady state, each averaged over 21 snapshots spanning 20 Myr (RBN: 266 to 286 Myr, and WSWb: 305 to 325 Myr) and the total simulation domain  $|z| \leq 1.12 \text{ kpc}$ . The smaller frames to the right display the same information but near the midplane,  $|z| < 20 \text{ pc}$ , only.

Model WSWa, with half the resolution and  $|z| \leq 2 \text{ kpc}$ . He reports average energy densities of 24 and  $10 E_{\text{SN}} \text{ kpc}^{-3}$  (thermal and kinetic, respectively) with SN rate =  $\dot{\sigma}_{\text{SN}}$ , comparable to 30 and  $13 E_{\text{SN}} \text{ kpc}^{-3}$  obtained here for Model WSWa.

Balsara et al. (2004) simulate an unstratified cubic region 200 pc in size, driven at SN rates of 8, 12 and 40 times the Galactic rate, with resolution more than double that of Model WSWa. For SN rates  $12\dot{\sigma}_{\text{SN}}$  and  $8\dot{\sigma}_{\text{SN}}$ , they obtain average thermal energy densities of about 225 and  $160 E_{\text{SN}} \text{ kpc}^{-3}$ , and average kinetic energy densities of 95 and  $60 E_{\text{SN}} \text{ kpc}^{-3}$ , respectively (derived from their energy totals divided by the  $[200 \text{ pc}]^3$  volume).

To allow comparison with our models, where the SNe energy injection rate is  $1\dot{\sigma}_{\text{SN}}$ , if we divide their energy densities by 12 and 8, respectively, the energy densities would be 19 and  $20 E_{\text{SN}} \text{ kpc}^{-3}$  (thermal), and 8 and  $7.5 E_{\text{SN}} \text{ kpc}^{-3}$  (kinetic). These are slightly lower than our results with RBN cooling ( $25$  and  $9 E_{\text{SN}} \text{ kpc}^{-3}$ ), but are below those with WSW ( $30$  and  $13 E_{\text{SN}} \text{ kpc}^{-3}$  for WSWa, as given above). Balsara et al. (2004) used an alternative cooling function (Raymond & Smith 1977), so allowing for some additional uncertainty over the net radiative energy losses, the results appear remarkably consistent.

While cooling and resolution may marginally affect the magnitudes, it appears that thermal energy density may consistently be expected to be about 2.5 times the kinetic energy density, in these

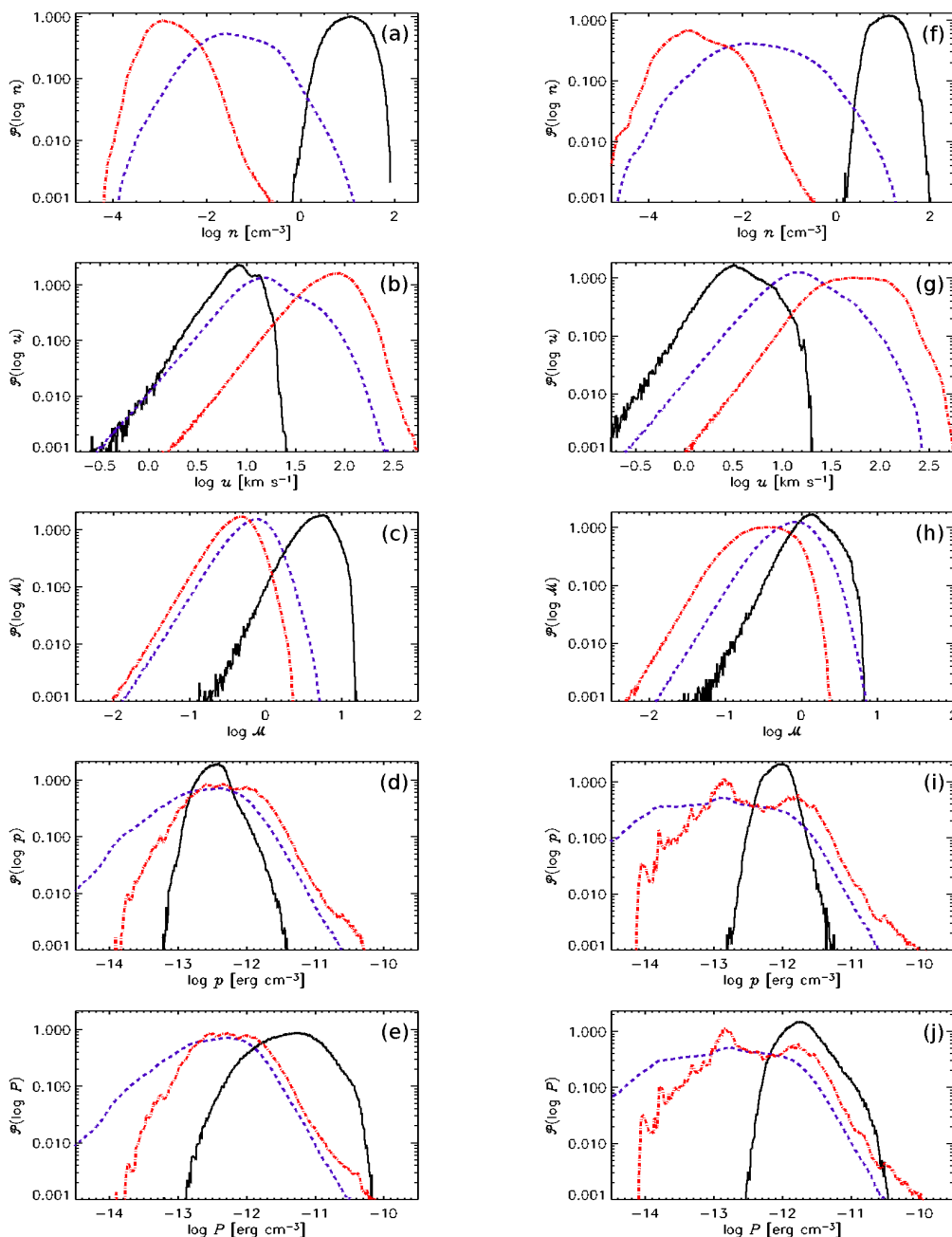


**Figure 15.** Probability densities for various variables in individual phases, for Model WSWb (left-hand column of panels) and Model RBN (right-hand column): (a) and (f) for gas density; (b) and (g) for random velocity  $u_0$ ; (c) and (h) for the Mach number of the random velocity defined with respect to the local sound speed; (d) and (i) for thermal pressure; and (e) and (j) for the total pressure. The cold phase spans  $T < 500$  K (black, solid), the warm gas has  $500 < T < 5 \times 10^5$  K (blue, dashed) and the hot gas is at  $T \geq 5 \times 10^5$  K (red, dash-dotted). Eleven snapshots have been used for averaging, spanning  $t = 200\text{--}300$  Myr for Model RBN and  $t = 300\text{--}400$  Myr for Model WSWb.

models. It also appears, by comparing the stratified and unstratified models, that the ratio of thermal to kinetic energy is not strongly dependent on height over the range included in our model.

The two models are further compared in Fig. 14, where we show probability distributions for the gas density, temperature and thermal pressure. With both cooling functions, the most probable gas number density is around  $3 \times 10^{-2} \text{ cm}^{-3}$ ; the most probable temperatures are also similar, at around  $3 \times 10^4$  K. With the RBN cooling function, the density range extends to smaller densities than with WSWb; and yet the temperature range for WSWb extends to

lower values than for RBN. It is evident that the isobarically unstable part of the WSW cooling function does significantly reduce the amount of gas at  $T = 313\text{--}6102$  K (the temperature range corresponding to the thermally unstable regime of the WSW cooling), and increase the amount of gas below 100 K. However this is not associated with higher densities than when using the RBN cooling function. This may indicate that multiple compressions, rather than thermal instability, dominate the formation of dense clouds.

The most probable thermal pressure is lower in Model RBN

than in WSWb, consistent with the lower thermal energy content of the former.

The probability distributions of various quantities, shown in Fig. 15, confirm the clear phase separation in terms of gas density and perturbation velocity. Here we used the same borderline temperatures for individual phases as for Model WSWa (Fig. 5). Despite minor differences between the corresponding panels in Figs. 5 and 15, the peaks in the gas density probability distributions are close to  $10^1, 3 \times 10^{-2}$  and  $10^{-3} \text{ cm}^{-3}$  in all models. Given the extra cooling of hot gas and reduced cooling of cold gas with the RBN cooling function, more of the gas resides in the warm phase in Model RBN. The thermal pressure distribution in the hot gas reveals the two ‘types’ (see the end of section 4), which are mostly found within  $|z| \lesssim 200 \text{ pc}$  (high pressure hot gas within SN remnants) and outside this layer (diffuse, lower pressure hot gas). The probability distribution for the Mach number in the warm gas extends to higher values with the RBN cooling function, perhaps because more shocks reside in the more widespread warm gas, at the expense of the cold phase. It is useful to remember that, although each distribution is normalised to unit underlying area, the fractional volume of the warm gas is about a hundred times that of the cold phase.

The probability distributions of density and pressure in without preliminary separation into phases, presented in Fig. 14 do not show clear separations into phases (cf. e.g. Joung & Mac Low 2006; de Avillez & Breitschwerdt 2004), such that division into three phases would arguably only be conventional, if based on these alone. The probability distributions near the mid-plane,  $|z| < 20 \text{ pc}$  Fig. 14, exhibit a marginally better phase separation for the gas density (smaller frames in Fig. 14) (see also Korpi et al. 1999; Hill et al. 2012, their Figs. 1; and 6, respectively). However our analysis in terms of phase-wise PDFs confirms that the trimodal structure evident in the temperature distribution (Fig. 14b) has a complementary structure in the gas density.

Stratification of the thermal structure is clarified in Fig. 16, where we introduce narrower temperature bands specified in Table 6. The fractional volume of gas in each temperature range  $i$  at a height  $z$  is given by

$$f_{V,i}(z) = \frac{V_i(z)}{V(z)} = \frac{N_i(z)}{N(z)}, \quad (31)$$

similarly to Eq. (14), where  $N_i(z)$  is the number of grid points in the temperature range  $T_{i,\min} \leq T < T_{i,\max}$ , with  $T_{i,\min}$  and  $T_{i,\max}$  given in Table 6, and  $N(z)$  is the total number of grid points at that height.

The fractional volumes in Column (13) of Table 3 show that near the mid-plane cold gas forms in similar abundances, independent of the cooling function. However, much less hot gas is achieved for Model RBN. Figure 16 also helps show how the thermal gas structure depends on the cooling function. Model WSWb, panel (b), has significantly more very cold gas ( $T < 50 \text{ K}$ ) than RBN, panel (a), but slightly warmer cold gas ( $T < 500 \text{ K}$ ) is more abundant in RBN. The warm and hot phases ( $T > 5 \times 10^3 \text{ K}$ ) have roughly similar distributions in both models, although Model RBN has less of both phases. Apart from relatively minor details, the effect of the form of the cooling function thus appears to be straightforward and predictable: stronger cooling means more cold gas and vice versa. What is less obvious, however, is that the very hot gas is more abundant near  $\pm 1 \text{ kpc}$  in Model RBN than in WSWb, indicating that the typical densities must be much lower. This, together with the greater abundance of cooler gas near the mid-plane, suggest that there is less stirring with RBN cooling.

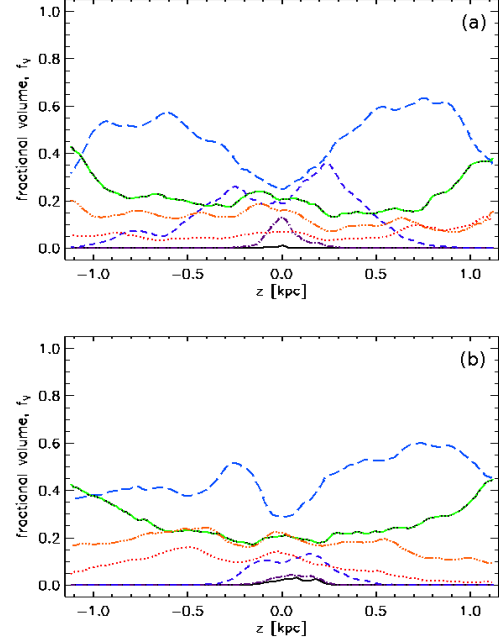


**Figure 16.** Vertical profiles of the fractional volumes occupied by the various temperature ranges, with the key shown in Table 6. (a) Model RBN, using 21 snapshots spanning 266 to 286 Myr. (b) Model WSWb, using 21 snapshots spanning 305 to 325 Myr.

**Table 6.** Key to Figs 16 and 17, defining the gas temperature bands used there, and the classification within three phases.

Temperature band	Line style	Phase
$T < 5 \times 10^1 \text{ K}$	—	cold
$5 \times 10^1 \text{ K} \leq T < 5 \times 10^2 \text{ K}$	- - - -	cold
$5 \times 10^2 \text{ K} \leq T < 5 \times 10^3 \text{ K}$	- - - -	warm
$5 \times 10^3 \text{ K} \leq T < 5 \times 10^4 \text{ K}$	- - - -	warm
$5 \times 10^4 \text{ K} \leq T < 5 \times 10^5 \text{ K}$	- - - -	warm
$5 \times 10^5 \text{ K} \leq T < 5 \times 10^6 \text{ K}$	- - - -	hot
$T \geq 5 \times 10^6 \text{ K}$	- - - -	hot

Altogether, we conclude that the properties of the cold and warm phases are not strongly affected by the choice of the cooling function. The main effect is that the RBN cooling function produces less hot gas with significantly lower pressures. This can readily be understood, as this function provides significantly stronger cooling at  $T \gtrsim 10^3 \text{ K}$ .

## 8.2 The total gas mass

Models RBN and WSWb have about 17% more mass of gas than the reference Model WSWa, where we have removed that part of the gas mass which should be confined to molecular clouds unresolved in our simulations (as described in section 3). The difference is apparent in comparing Fig. 16b with Fig. 17b (or Fig. 17a). Higher gas mass causes the abundance of hot gas to reduce with height, contrary to observations, and to the behaviour of Model WSWa. Otherwise, the fractional volumes within  $\pm 200 \text{ pc}$  of the mid-plane appear independent of the gas mass.

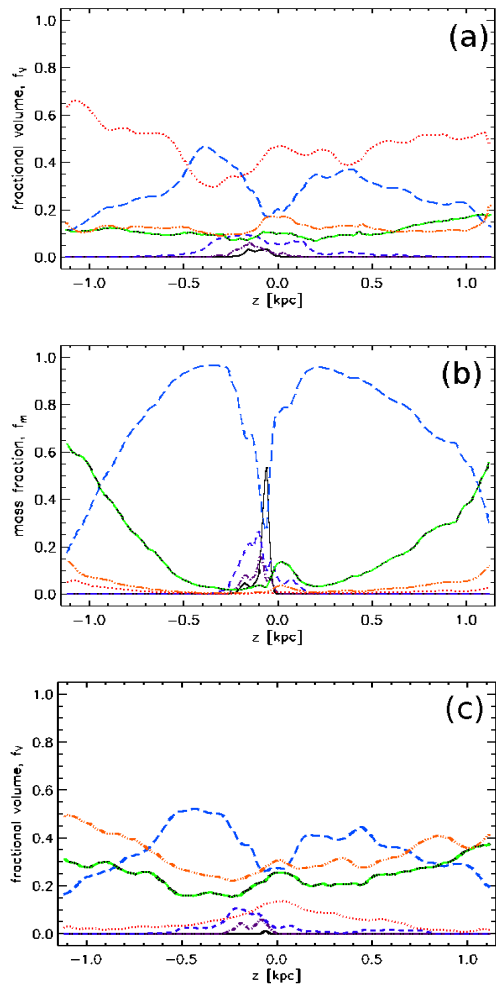


**Figure 17.** Vertical profiles of the fractional volumes (Eq. 14) for Model WSWah (a), which differs only in its doubled spatial resolution from the reference Model WSWa (c) and the fractional mass (Eq. 32) from Model WSWa (b). These are calculated for the temperature ranges given, along with the figure legend, in Table 6. The former uses 10 snapshots and the latter 6 spanning 633 to 638 Myr.

### 8.3 Numerical resolution

Models WSWa and WSWah differ only in their resolution, using 2 and 4 pc, respectively. Model WSWah is a continuation of the state of WSWa after 600 Myr of evolution.

The most obvious effect of increased resolution is the increase in the magnitude of the perturbed velocity and temperatures;  $\langle u_{\text{rms}} \rangle = 76 \text{ km s}^{-1}$  in Model WSWa increasing to  $103 \text{ km s}^{-1}$  in Model WSWah (Table 3, Column 9) and  $\langle c_s \rangle$  from  $150$  to  $230 \text{ km s}^{-1}$  (Column 6). Both  $\langle u_{\text{rms}} \rangle$  and the random velocity  $\langle u_{0,\text{rms}} \rangle$  are increased by a similar factor of about 1.3. However, the thermal energy  $e_{\text{th}}$  is reduced by a factor of 0.6 with the higher resolution, while kinetic energy  $e_{\text{k}}$  remains about the same. This suggests that in the higher-resolution model, the higher velocities and temperatures are associated with lower gas densities.

The vertical distribution of the fractional volume in each temperature range (defined in Table 6) is shown in Fig. 17 for Model WSWah (panel a) for comparison with Model WSWa in

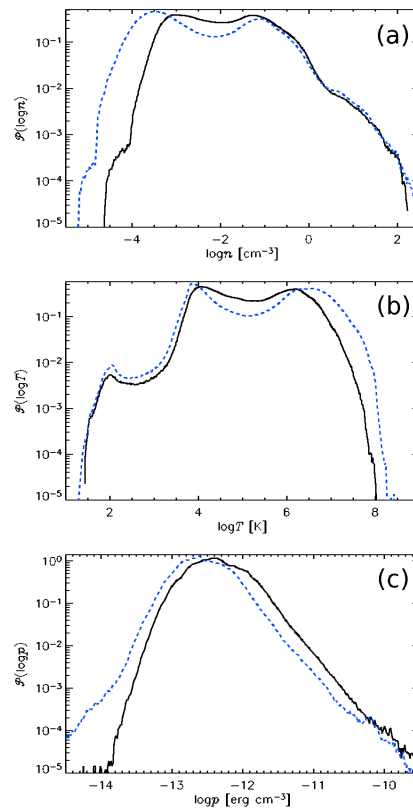


**Figure 18.** Volume weighted probability distributions of gas number density (a), temperature (b) and thermal pressure (c) for models WSWa (black, solid) and WSWah (blue, dashed) for the total numerical domain  $|z| \leq 1.12 \text{ kpc}$ .

(c). The fractional mass (b) is calculated similarly to Eq. (31) is

$$f_{M,i}(z) = \frac{M_i(z)}{M(z)}, \quad (32)$$

where  $M_i(z)$  is the mass of gas within temperature range  $i$  at a given  $z$ , and  $M(z)$  is the total gas mass at that height.

Note that the relative abundances of the various phases in these models might be affected by the unrealistically high thermal conductivity adopted. The coldest gas (black, solid), with  $T < 50 \text{ K}$ , is largely confined within about 200 pc of the mid-plane. Its fractional volume (Fig. 17a,c) is small even at the mid-plane, but it provides more than half of the gas mass at  $z = 0$  (Fig. 17b). Gas in the next temperature range,  $50 < T < 500 \text{ K}$  (purple, dash-dotted), is similarly distributed in  $z$ . Models WSWa and WSWah differ only in their resolution, using 2 and 4 pc, respectively. Model WSWah is a continuation of the state of WSWa after 600 Myr of evolution. With higher resolution the volume fraction of the coldest gas is significantly enhanced (Fig. 17c compared to a), but it is similarly distributed.

Gas in the range  $5 \times 10^2 < T < 5 \times 10^3 \text{ K}$  (dark blue, dashed) has a similar profile to the cold gas for both the fractional mass and the fractional volume, and this is insensitive to the model resolution. This is identified with the warm phase, but exists in the thermally unstable temperature range. It accounts for about 10% by volume and 20% by mass of the gas near the mid-plane, which is consistent with observational evidence. It is negligible away from the supernova active regions.

The two bands with  $T > 5 \times 10^5 \text{ K}$  (red, dotted and or-

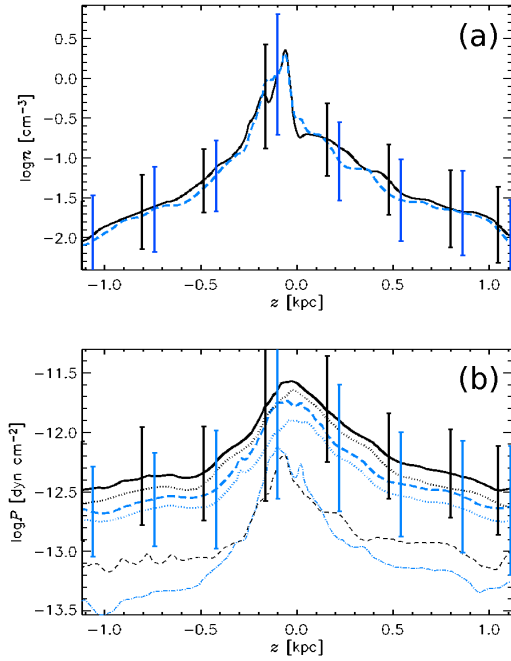


**Figure 19.** Horizontal averages of gas number density,  $\bar{n}(z)$  (a), and total pressure,  $P(z)$  (b), for Model WSWa (solid, black), and Model WSWah (dashed, blue). Each are time-averaged using 6 and 10 snapshots respectively, spanning 633 to 638 Myr. The vertical lines indicate standard deviation within each horizontal slice. The thermal  $p(z)$  (dotted) and ram  $p_0(z)$  (fine dashed) pressures are also plotted (b).

ange, dash-3dotted) behave similarly to each other (Fig. 17a,c), occupying similar fractional volumes for  $|z| \lesssim 0.75$  kpc, and with  $f_{V,i}$  increasing above this height (more rapidly for the hotter gas). In contrast the fractional masses (Fig. 17b) in these temperature bands are negligible for  $|z| \lesssim 0.75$  kpc, and increase above this height (less rapidly for the hotter gas). The temperature band  $5 \times 10^4 < T < 5 \times 10^5$  K (green/black, dash-3dotted) is similarly distributed to the hotter gas (orange) in all profiles. It is however identified with the warm phase, indicating that this is mainly hot gas cooling, a transitional state, which accounts for a relatively small volume fraction of the warm gas and especially a small mass fraction. The dramatic effect of increased resolution (Fig. 17a compared to c) is the significant increase in the very hot gas (red, dotted), particularly displacing the hotter gases (orange and green) but also to some degree the bulk warm gas (blue, dashed). This reflects the reduced cooling due to the better density contrasts resolved, associating the hottest temperatures to the most diffuse gas.

The middle temperature range  $5 \times 10^3 < T < 5 \times 10^4$  K has a distinctive profile in both fractional volume and fractional mass, with minima near the mid-plane and maxima at about  $|z| \simeq 400$  pc, being replaced as the dominant component by hotter gas above this height. The fractional volume and vertical distribution of this gas is quite insensitive to the resolution. The distribution of the warm gas ( $5 \times 10^3$  K  $\leq T < 5 \times 10^4$  K; blue, long-dashed) does not change much with increased resolution. However, the higher-resolution model has more of the cold phase ( $T < 500$  K; black, solid and dash-dotted) and, especially, of the very hottest gas ( $T \geq 5 \times 10^6$  K; red, dotted), at the expense of the intermediate temperature ranges.

This can also be seen in the gas density and temperature prob-

ability distributions shown in Fig. 18(a), (b): increased resolution modestly increases the abundance of cold gas and significantly enhances the amount of very hot gas. The minima in the distributions (at density  $10^{-2}$  cm $^{-3}$ , and at temperatures  $10^2$  and  $3 \times 10^5$  K) appear independent of resolution, suggesting that the phase separation is physical, rather than numerical. The distributions are most consistent in the thermally unstable range 313–6102 K. Higher resolution also reduces the minimum further about the unstable range above  $10^5$  K, as the highest temperature gas has lower losses to thermal conduction. The mean temperatures of the cold gas (60 K) warm gas ( $10^4$  K) and the mean warm gas density ( $0.14$  cm $^{-3}$ ) also appear to be independent of the resolution. However the natural log mean  $\mu_n$  is about -8 for the hot gas, both within and without 2 pc of the mid-plane (with larger standard deviation for the gas near the mid-plane). This compares with values of -6.97 and -5.78 in our model with 4 pc resolution; i.e. a factor of about 1/3. This reflects the improved resolution of low density in the remnant interiors.

The density and temperature probability distributions for WSWa are similar to those obtained by Joung & Mac Low (2006, their Fig. 7), who used a similar cooling function, despite the difference in the numerical methods (adaptive mesh refinement down to 1.95 pc in their case). With slightly different implementation of the cooling and heating processes, again with adaptive mesh refinement down to 1.25 pc, de Avillez & Breitschwerdt (2004, their Fig. 3) found significantly more cool, dense gas. It is noteworthy that the maximum densities and lowest temperatures obtained in our study with a non-adaptive grid are of the same order of magnitude as those from AMR-models where the local resolution is up to three times higher. At 4 pc our mean minimum temperature is 34 K, within the range 15–80 K for 0.625–2.5 pc (de Avillez & Breitschwerdt 2004, their Fig. 9). For mean maximum gas number, our  $122$  cm $^{-3}$  is within their range 288–79 cm $^{-3}$ .

The vertical density profiles obtained under the different numerical resolutions are shown in Fig. 19a. Although the density distribution in Fig. 18a reveals higher density contrasts with increased resolution, there is little difference in the  $z$ -profiles of the models. The mean gas number density at the mid-plane,  $n(0)$  — which with our course grid resolution excludes the contribution from HII — is about  $2.2$  cm $^{-3}$ : double the observation estimates summarised in Ferrière (2001). This might be expected in the absence of the magnetic and cosmic ray components of the ISM pressure, to help support the gas against the gravitational force.

However the vertical pressure distributions are consistent with the models of Boulares & Cox (1990, their Figs. 1 and 2), which include the weight of the ISM up to  $|z| = 5$  kpc. The total pressure  $P(0) \simeq 2.5 (2.0) \times 10^{-12}$  dyn cm $^{-2}$  for the standard (high) resolution model is slightly above their estimate of about 1.9 for hot, turbulent gas. For the turbulent pressure alone we have  $p_0(0) \simeq 6.3 (7.9) \times 10^{-13}$  dyn cm $^{-2}$  falling to 1.0 (0.6) at  $|z| = 500$  pc and then remaining reasonably level. The pressures are generally slightly reduced with increased resolution, except for  $p_0$  near the mid-plane. Small scales are better resolved, so the turbulent structures are a stronger component of the SN active region. These pressures are consistent with Boulares & Cox (1990), even though our model does not explicitly include the pressure contributions from the ISM above 1 kpc.

Comparing our thermal pressure distribution (Fig. 18c) with de Avillez & Breitschwerdt (2004, their Fig. 4a) and Joung et al. (2009, their Fig. 2), the three models peak at 3.16, 1.3 and  $4.1 \times 10^{-13}$  dyn cm $^{-2}$ , respectively. The latter models include  $|z| = 10$  kpc and resolution up to 1.25 pc. Our data summarise the vol-

ume within  $z \pm 1$  kpc, while the comparisons are within 10 kpc and 125 pc respectively.

We conclude that the main effects of the increased resolution are confined to the very hot interiors and to the thin shells of SN remnants; the interiors become hotter and the SN shell shocks become thinner with increased resolution (see Appendix B). Simultaneously, the higher density of the shocked gas enhances cooling, producing more cold gas and reducing the total thermal energy. Otherwise, the overall structure of the diffuse gas is little affected: the probability distributions of thermal pressure are almost indistinguishable, with our standard resolution fractionally higher pressure (Fig. 18c).

We are satisfied that the numerical resolution of the reference model,  $\Delta = 4$  pc, is sufficient to model the diffuse gas phases reliably. This choice of the working numerical resolution is further informed by tests involving the expansion of individual SN remnants (presented in Appendix B).

## 9 DISCUSSION AND CONCLUSIONS

The multi-phase gas structure obtained in our simulations appears to be robust, with overall parameters relatively insensitive to the physical (Section 4) and numerical (Section 8.3) details, including the parameterizations of the radiative cooling tested here (Section 8.1). We have identified natural temperature boundaries of the major phases using the variation, with height above the mid-plane, of the fractional volume occupied by the gas in relatively narrow temperature ranges. This confirms that the system can be satisfactorily described in terms of just three major phases with temperature ranges  $T < 5 \times 10^2$  K,  $5 \times 10^2 \leq T < 5 \times 10^5$  K and  $5 \times 10^5 \leq T < 5 \times 10^6$  K. The most probable values of the variables we have explored (gas density, thermal and total pressure, perturbed velocity and Mach number) are practically independent of the cooling function chosen (Fig. 15). Moreover, this is true for the cold, warm and hot phases separately. A 3D rendering of a snapshot of the density distribution from the reference model WSWa is illustrated in Fig 20, showing the typical location and density composition of each phase separately.

A conspicuous contribution to various diagnostics — especially within 200 pc of the mid-plane, where most of the SNe are localised — comes from the very hot gas within SN remnants. Regarding its contribution to integrated gas parameters, it should perhaps be considered as a separate phase.

The fractional volume occupied by each phase is a convenient diagnostic and an important physical parameter. We have clarified the relation between the fractional volume and various probabilistic measures of a random distribution of density (or of any other quantity), and established an exact relation between the fractional volume and various density averages obtainable observationally (in Section 5). This represents a significant improvement upon the assumption of locally homogeneous gas, the only analytical tool used to date in determinations of the fractional volumes of the phases.

The correlation scale of the random flows is obtained in Section 6, from the autocorrelation functions of the velocity components. Within 200 pc of the mid-plane, the horizontal velocity components have a consistent correlation scale of about 100 pc. In contrast, the scale of the vertical velocity (which has a systematic part due to the galactic outflow of hot gas) grows from about 100 pc at the mid-plane to nearly 200 pc at  $z = 200$  pc, and may do so further at larger heights (cf. Korpi et al. 1999). This is due to the increase of the fractional volume of the hot gas with distance from

the mid-plane. At  $|z| \simeq 1$  kpc most of the volume is occupied by the hot gas. As the interstellar gas flows out of the galactic disc into the halo, it must expand, and the scale of the expanding regions may be expected to become comparable to 1 kpc at  $|z| \simeq 1$  kpc. It would be helpful to obtain estimates of the horizontal correlation of the flow above  $\pm 1$  kpc, so that modelling of the galactic fountain might be adequately formulated.

We find clear indication of cold gas falling back towards the mid-plane at speeds of a few km/s, hot gas involved in vigorous outflow away from the mid-plane, and some warm gas entrained in this outflow (Section 7). The outflow speed of the hot gas increases up to  $100 \text{ km s}^{-1}$  within 100 pc of the mid-plane and then slowly decreases. In contrast, the mean vertical velocity of the warm gas increases linearly with  $|z|$ , up to  $20 \text{ km s}^{-1}$  towards the upper boundaries of our domain.

Given that probability densities for gas temperature and number density, calculated for individual phases, are clearly separated, the probability densities for both thermal and total pressure (the sum of thermal and turbulent) are not segregated at all. Despite its complex thermal and dynamical structure, the gas is in statistical pressure equilibrium. Since the SN-driven ISM is random in nature, both total and thermal pressure fluctuate strongly in both space and time (albeit with significantly smaller relative fluctuations than the gas density, temperature and perturbation velocity), so the pressure balance is also statistical in nature. These might appear to be obvious statements, since a statistical steady state (i.e., not involving systematic expansion or compression) must have such a pressure balance. Deviations from *thermal* pressure balance and observations of significant regions of gas within the classically forbidden thermally unstable range (300 – 6000 K), which is also evident in our probability distributions, may lead to conclusions of an ISM comprising a broad thermodynamic continuum in pressure disequilibrium (Vázquez-Semadeni 2012, discussion on *The controversy*). The only systematic deviations from pressure balance are associated with the systematic outflow of the hot gas (leading to lower pressures), and with the compression of the cold gas by shocks and other converging flows (leading to somewhat increased pressures). Even this can be further reconciled if we allow for the global vertical pressure gradient (cf. Fig. 7). It is evident that phases are locally in total pressure equilibrium.

An important technical aspect of simulations of this kind is the minimum numerical resolution  $\Delta$  required to capture the basic physics of the multi-phase ISM. We have shown that  $\Delta = 4$  pc is sufficient with the numerical methods employed here (Section 8.3). In addition to comparing results obtained for  $\Delta = 4$  pc and 2 pc with our own code, we have satisfied ourselves that our results are consistent with those obtained by other authors using adaptive mesh refinement with maximum resolutions of 2 pc and 1.25 pc.

As with all other simulations of the SN-driven ISM, we employ a host of numerical tools (such as shock-capturing diffusivity) to handle the extremely wide dynamical range ( $10^2 \lesssim T \lesssim 10^8$  K and  $10^{-4} \lesssim n \lesssim 10^2 \text{ cm}^{-3}$  in terms of gas temperature and number density in our model) and widespread shocks characteristic of the multi-phase ISM driven by SNe. Their detailed description can be found in Section 2.4. We have carefully tested our numerical methods by reproducing, quite accurately, the Sedov–Taylor and snowplough analytical solutions for individual SN remnants (Appendix B).

The major elements of the ISM missing from the models presented here are magnetic fields and cosmic rays. Analysis of the structure of the velocity field and its interaction with the magnetic

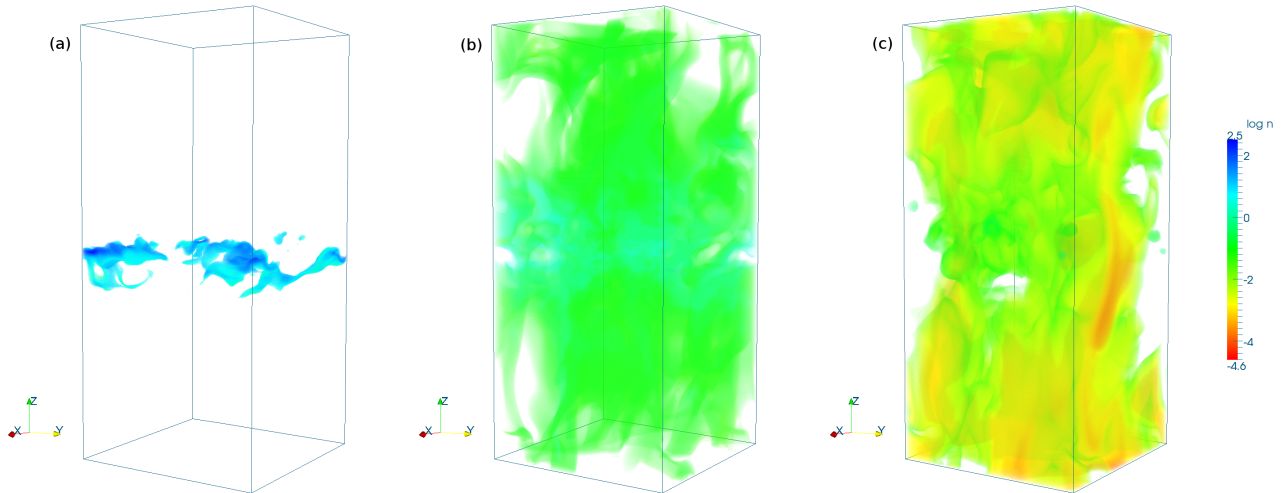


**Figure 20.** 3D snapshots, from model WSWa, of gas number density in (a) the cold gas, (b) the warm gas, and (c) the hot gas. In each plot regions that are clear (white space) contain gas belonging to another phase. The phases are separated at temperatures 500 K and  $5 \times 10^5$  K. The colour scale for  $\log n$  is common to all three plots.

field, effects of rotation, shear and SN rates will be the subject of a future paper.

## ACKNOWLEDGEMENTS

Part of this work was carried out under the programme HPC-EUROPA2 of the European Community (Project No. 228398) – Research Infrastructure Action of the FP7. We gratefully acknowledge the resources and support of the CSC-IT Center for Science Ltd., Finland, where the major part of the code adjustment and all of the final simulations were carried out. The contribution of Jyrki Hokkanen (CSC) to enhancing the graphical representation of the results is gratefully acknowledged. We used the UK MHD Computer Cluster in St Andrews, Scotland, for code development and testing. MJM is grateful to the Academy of Finland for support under Projects 218159 and 141017. The work of AF, GRS and AS has been supported by the Leverhulme Trust’s Research Grant RPG-097 and the STFC grant F003080. FAG has been supported by the EPSRC DTA grant to the Newcastle University. We thank Elly Berkhuijsen for insightful comments on filling factors and the anonymous referee for their conscientious and constructive contribution.

## APPENDIX A: NOTATION

Table A1 contains most of the symbols used in the text and their explanation, arranged alphabetically.

## APPENDIX B: EVOLUTION OF AN INDIVIDUAL SUPERNOVA REMNANT

The thermal and kinetic energy supplied by SNe drives, directly or indirectly, all the processes discussed in this paper. It is therefore crucial that the model captures correctly the energy conversion in the SN remnants and its transformation into the thermal and kinetic energies of the interstellar gas. As discussed in Section 2.2, the size of the region where the SN energy is injected corresponds to the

adiabatic (Sedov–Taylor) or the snowplough stage. Given the multitude of artificial numerical effects required to model the extreme conditions in the multi-phase ISM, it is important to verify that the basic physical effects are not affected, while sufficient numerical control of strong shocks, rapid radiative cooling, supersonic flows, etc., is properly ensured. Another important parameter to be chosen is the numerical resolution.

Before starting the simulations of the multi-phase ISM reported in this paper, we have carefully confirmed that the model can reproduce, to sufficient accuracy, the known realistic analytical solutions for the late stages of SN remnant expansion, until merger with the ISM. The minimum numerical resolution required to achieve this in our model is  $\Delta = 4$  pc. In this Appendix, we consider a single SN remnant, initialised as described in Section 2.2, that expands into a homogeneous environment. All the numerical elements of the model are in place, but here we use periodic boundary conditions in all dimensions.

The parameters  $\chi_1$  and  $\nu_1$  are as applied in Model WSWa for  $\Delta = 4$  pc, but reduced here proportionally for  $\Delta = 2$  and 1 pc. The constant  $C \approx 0.01$  used in Eq. (10) to suppress cooling around shocks is unchanged. This may allow excess cooling at higher resolution, evident in the slightly reduced radii in Fig. B1. For Model WSWah,  $\chi_1$  and  $\nu_1$  were just as in Model WSWa; for future reference, they should be appropriately adjusted, as should  $C$ , to better optimise higher resolution performance.

## B1 The adiabatic and snowplough stages

The Sedov–Taylor solution,

$$R = \left( \kappa \frac{E_{\text{SN}}}{\rho_0} \right)^{1/5} t^{2/5}, \quad (\text{B1})$$

is accurately reproduced with our code at the resolution  $\Delta = 4$  pc or higher. Here  $R$  is the remnant radius,  $E_{\text{SN}}$  the explosion energy,  $\rho_0$  the ambient gas density, and  $\kappa \approx 2.026$  for  $\gamma = 5/3$  (Ostriker & McKee 1988).

Modelling even a single remnant becomes more challenging when radiative cooling becomes important. Here we compare numerical results with two analytic solutions for an SN remnant ex-

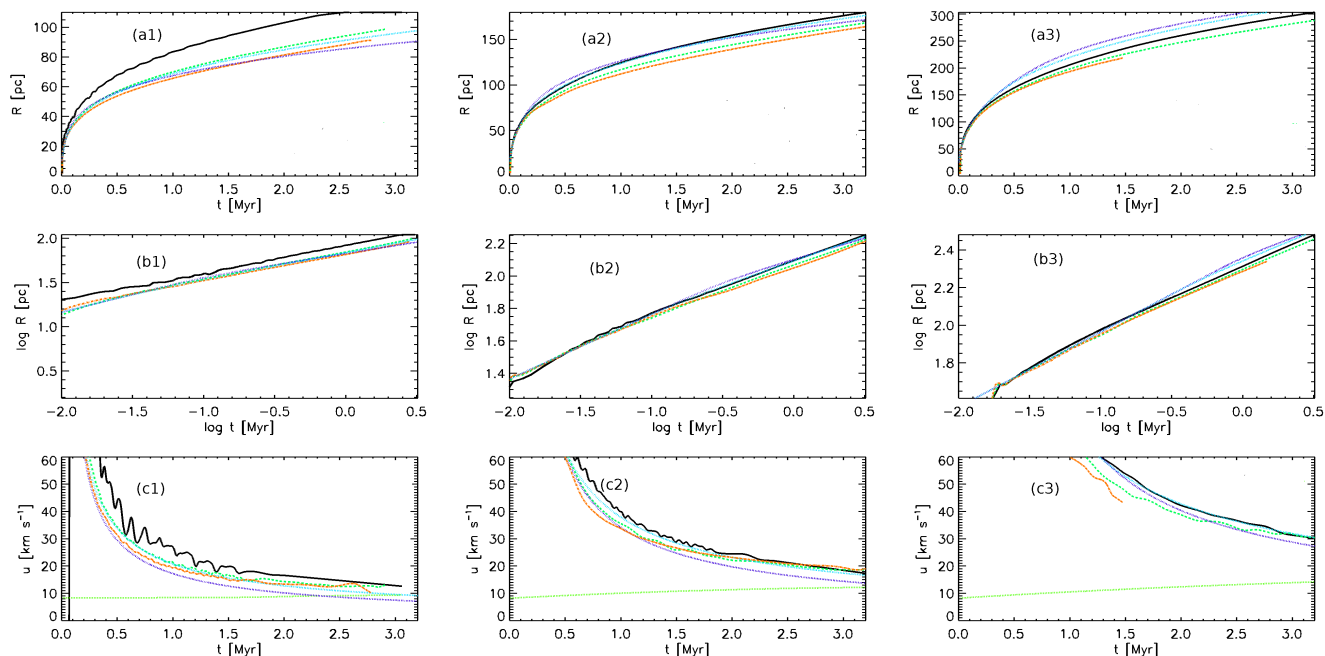


**Figure B1.** The shell radius  $R$  of an SN remnant versus time, shown in (a) linear and (b) logarithmic scales; (c) the corresponding expansion speed  $\dot{R}$ . Frame columns 1–3 are for different ambient gas densities,  $\rho_0 \times 10^{24} \text{ g cm}^{-3} = 1.0, 0.1, 0.01$  from left to right. Numerical results obtained under three numerical resolutions are shown:  $\Delta = 4 \text{ pc}$  (black, solid),  $2 \text{ pc}$  (green, dashed) and  $1 \text{ pc}$  (orange, dash-dotted). Dotted lines are for the standard snowplough solution (B2) (dark blue) and its modification by Cioffi et al. (1998) (light blue). The horizontal line in Panels (c1)–(c3) shows the sound speed in the ambient ISM.

panding into a perfect, homogeneous, monatomic gas at rest. The standard momentum-conserving snowplough solution for a radiative SN remnant has the form

$$R = R_0 \left[ 1 + 4 \frac{\dot{R}_0}{R_0} (t - t_0) \right]^{1/4}, \quad (\text{B2})$$

where  $R_0$  is the radius of the SN remnant at the time  $t_0$  of the transition from the adiabatic stage, and  $\dot{R}_0$  is the shell expansion speed at  $t_0$ . The transition time is determined by Woltjer (1972) as that when half of the SN energy is lost to radiation; this happens when

$$\dot{R}_0 = 230 \text{ km s}^{-1} \left( \frac{n_0}{1 \text{ cm}^{-3}} \right)^{2/17} \left( \frac{E_{\text{SN}}}{10^{51} \text{ erg}} \right)^{1/17}; \quad (\text{B3})$$

the transitional expansion speed thus depends very weakly on parameters.

Cioffi et al. (1998) obtained numerical and analytical solutions for an expanding SN remnant with special attention to the transition from the Sedov–Taylor stage to the radiative stage. These authors adjusted an analytical solution for the pressure-driven snowplough stage to fit their numerical results to an accuracy of within 2% and 5% in terms of  $R$  and  $\dot{R}$ , respectively. (Their numerical resolution was  $0.1 \text{ pc}$  in the interstellar gas and  $0.01 \text{ pc}$  within ejecta.) They thus obtained

$$R = R_p \left( \frac{4}{3} \frac{t}{t_p} - \frac{1}{3} \right)^{3/10}, \quad (\text{B4})$$

where the subscript p denotes the radius and time for the transition to the pressure driven stage. The estimated time of this transition is

$$t_p \simeq 13 \text{ Myr} \left( \frac{E_{\text{SN}}}{10^{51} \text{ erg}} \right)^{3/14} \left( \frac{n_0}{1 \text{ cm}^{-3}} \right)^{-4/7}.$$

For ambient densities of  $\rho_0 = (0.01, 0.1, 1) \times 10^{-24} \text{ g cm}^{-3}$ ,

this yields transition times  $t_p \approx (25, 6.6, 1.8) \times 10^4 \text{ yr}$  and shell radii  $R_p \approx (130, 48, 18) \text{ pc}$ , respectively, with speed  $\dot{R}_p = (213, 296, 412) \text{ km s}^{-1}$

This continues into the momentum driven stage with

$$\left( \frac{R}{R_p} \right)^4 = \frac{3.63 (t - t_m)}{t_p} \left[ 1.29 - \left( \frac{t_p}{t_m} \right)^{0.17} \right] + \left( \frac{R_m}{R_p} \right)^4, \quad (\text{B5})$$

where subscript m denotes the radius and time for this second transition,

$$t_m \simeq 61 t_p \left( \frac{\dot{R}_{\text{ej}}}{10^3 \text{ km s}^{-1}} \right)^3 \left( \frac{E_{\text{SN}}}{10^{51} \text{ erg}} \right)^{-3/14} \left( \frac{n_0}{1 \text{ cm}^{-3}} \right)^{-3/7},$$

where  $\dot{R}_{\text{ej}} \simeq 5000 \text{ km s}^{-1}$  is the initial velocity of the  $4M_{\odot}$  ejecta. For each  $\rho_0 = (0.01, 0.1, 1.0) \times 10^{-24} \text{ g cm}^{-3}$ , the transitions occur at  $t_m = (168, 16.8, 1.68) \text{ Myr}$ , and  $R_m = (1014, 281, 78) \text{ pc}$ , respectively. The shell momentum in the latter solution tends to a constant, and the solution thus converges with the momentum-conserving snowplough (B2); but, depending on the ambient density, the expansion may become subsonic and the remnant merge with the ISM before Eq. (B2) becomes applicable.

We compare our results with the momentum-conserving snowplough solution and those of Cioffi et al. in Fig. B1, testing our model with numerical resolutions  $\Delta = 1, 2$  and  $4 \text{ pc}$  for the ambient gas densities  $\rho_0 = (0.01, 0.1, 1.0, 2.0) \times 10^{-24} \text{ g cm}^{-3}$ . Shown in Fig. B1 are a linear plot of the remnant radius  $R$  versus time to check if its magnitude is accurately reproduced, a double logarithmic plot of  $R(t)$  to confirm that the scaling is right, and variation of the expansion speed with time to help assess more delicate properties of the solution. We are satisfied to obtain good agreement with the analytical results for all the resolutions investigated when the ambient gas number density is below  $1 \text{ cm}^{-3}$ . For

**Table A1.** Most important variables used in the text.

Symbol	Meaning
$c_s$	Adiabatic speed of sound
$c_p$	Heat capacity at constant pressure [ $\text{kpc}^2 \text{Gyr}^{-3} \text{K}^{-1}$ ]
$C$	Velocity autocorrelation function, Eq. (29)
$D/Dt$	Advective derivative, Eq. (5)
$\mathcal{D}$	Velocity structure function, Eq. (28)
$e_{\text{th}}$	Energy density, subscript thermal: ‘th’, kinetic: ‘kin’
$E_{\text{SN}}$	Total energy injected into the ISM by a single SN
$f_{M,i}$	Fractional mass of gas in phase $i$ , Eq. (32)
$f_{V,i}$	Fractional volume occupied by the phase $i$ , Eq. (14)
$g_z$	Vertical acceleration due to the Galactic gravity, Eq. (7)
$h_{\text{I}}$	Scale height of the Type I SN distribution, Section 2.2
$h_{\text{II}}$	Scale height of the Type II SN distribution, Section 2.2
$k_{\text{B}}$	Boltzmann’s constant
$K$	Thermal conductivity ( $= c_p \rho \chi$ )
$l_0$	Velocity correlation scale
$m_p$	Proton mass
$\mathcal{M}$	Mach number
$n$	Gas number density
$\bar{n}_i$	Gas density averaged within a given phase $i$ , Eq. (17)
$\langle n_i \rangle$	Gas density averaged over volume $V$ of phase $i$ , Eq. (18)
$p$	Thermal pressure
$P$	Total pressure (thermal plus turbulent)
$\mathcal{P}$	Probability density
$r_{\text{SN}}$	Characteristic radius of the SN energy injection site, Section 2.2
rms	Root-mean square
$s$	Specific entropy, [ $\text{erg g}^{-1} \text{K}^{-1}$ ]
$s_n$	Parameter of the lognormal probability distribution, Eq. (13)
$S$	Velocity shear rate due to differential rotation
SN	Supernova (also as a subscript)
$T$	Gas temperature
$V$	Total volume of a region in Section 5.1
$V_i$	Volume occupied by an ISM phase labelled $i$ , Section 5.1
$\mathbf{u}$	Velocity perturbation: deviation of the gas velocity from the background rotational flow
$\mathbf{u}_0$	Random velocity, p. 3
$\mathbf{U}$	Large-scale shear flow (differential rotation), p. 3
$\mathbf{W}$	Rate of strain tensor, Eq. (4)
$\Gamma$	Specific rate of photoelectric heating, [ $\text{erg g}^{-1} \text{s}^{-1}$ ]
$\Delta$	Numerical mesh separation (resolution of a simulation)
$\zeta_\nu$	Shock-capturing viscosity
$\zeta_\chi$	Shock-capturing thermal diffusivity
$\Lambda$	Radiative cooling rate, [ $\text{erg g}^{-2} \text{s}^{-1} \text{cm}^{-3}$ ]
$\mu$	Molecular weight
$\mu_n$	Parameter of the lognormal probability distribution, Eq. (13)
$\nu$	Kinematic viscosity
$\nu_{\text{I}}$	Type I SN rate per unit surface area, Section 2.2
$\nu_{\text{II}}$	Type II SN rate per unit surface area, Section 2.2
$\Omega$	Angular velocity of the Galactic rotation
$\phi_i$	Phase filling factor within the ISM phase $i$ , Eq. (15)
$\Phi_i$	Volume filling factor of the ISM phase $i$ , Eq. (16)
$\dot{\rho}_{\text{SN}}$	Rate of mass injection, per unit volume, by SNe, Section 2.2
$\rho$	Gas density
$\dot{\sigma}_{\text{SN}}$	Rate of energy injection by SNe (per unit volume), as kinetic energy in Eq. (2) and as thermal energy in Eq. (3), see Section 2.2
$\sigma_i^2$	Variance of ISM phase $i$ , Section 5
$\tau_{\text{cool}}$	Radiative cooling time
$\Phi$	Gravitational potential
$\chi$	Thermal diffusivity

$\Delta = 4 \text{ pc}$ , the remnant radius is accurate to within about 3% for  $\rho_0 = 10^{-25} \text{ g cm}^{-3}$  and underestimated by up to 6% for  $\rho_0 = 10^{-26} \text{ g cm}^{-3}$ . At higher numerical resolutions, the remnant radius is underestimated by up to 7% and 11% for  $\rho_0 = 10^{-25} \text{ g cm}^{-3}$  and  $10^{-26} \text{ g cm}^{-3}$ , respectively. For  $\rho_0 = 10^{-24} \text{ g cm}^{-3}$ , excellent agreement is obtained for the higher resolutions,  $\Delta = 1$  and  $2 \text{ pc}$ ; simulations with  $\Delta = 4 \text{ pc}$  overestimate the remnant radius by about 20–25% in terms of  $R$  and  $\dot{R}$  at  $t = 2 \text{ Myr}$ . We emphasize that a typical SN explosion site in the models described in the main part of the paper has an ambient density  $n_0 < 1 \text{ cm}^{-3}$  so that  $\Delta = 2$ , or  $4 \text{ pc}$  produce a satisfactory fit to the results, despite the much finer resolution of the simulations, of Cioffi et al.

The higher than expected expansion speeds into dense gas can be explained by the artificial suppression of the radiative cooling within and near to the shock front as described by Eq. (10). Our model reproduces the low density explosions more accurately because the shell density is lower, and radiative cooling is therefore less important.

## B2 The structure of the SN remnant

Cuts through the simulated SN remnant are shown in Fig. B2 for gas density, temperature and velocity, obtained for resolution  $\Delta = 4 \text{ pc}$  and with ambient density  $\rho_0 = 10^{-25} \text{ g cm}^{-3}$ . In the temperature and velocity panels, we also include the profile of the shock viscosity from Eq. (9) (black dotted line), scaled to fit each plot. The temperature panels also show where net cooling is applied to the remnant,  $T^{-1}(\Gamma - \rho\Lambda) < 0$  from Eq.(3) (blue dashed line), while the velocity panels also show the ambient sound speed (pink dashed lines). The top panel depicts the initial distributions, at  $t = 0$ , with which the mass of  $4M_\odot$  and  $5 \times 10^{50} \text{ erg}$  each of thermal and kinetic energy are injected. The other panels are for  $t = 0.72$  and  $1.02$  after the start of the evolution, from top to bottom, respectively; the actual simulation continued to  $t = 1.32 \text{ Myr}$ , when the remnant radius reached  $130 \text{ pc}$ .

The position of the peak of the density profile is used to determine the shell radius shown in Fig. B1. The Rankine–Hugoniot jump conditions are not very well satisfied with the numerical parameters used here. This is due to our numerical setup, essentially designed to control the shocks by spreading them sufficiently to be numerically resolvable in production runs that contain many interacting shocks and colliding SN shells. Better shock front profiles have been obtained with other choices of parameters and cooling control, and with better resolution. The density and temperature contrasts across the shock fronts are reduced by the shock smoothing, which inhibits the peak density and enhances gas density behind the shocks. In an isolated remnant, the peak gas number density does not exceed  $10 \text{ cm}^{-3}$ , but in the full ISM simulation we obtain densities in excess of  $100 \text{ cm}^{-3}$ , as a result of interacting remnants and highly supersonic flows.

The interior of the SN remnant, if more dense due to numerical smoothing about the shock profile, would cool unrealistically rapidly, so that the SN energy would be lost to radiation rather than agitate the ambient ISM. The centre panels in Fig. B1 clarify how the cooling suppression described in Eq. (10) reduces the cooling rate in the relatively homogeneous interior of the remnant, while still allowing rapid cooling in the dense shell where the gradient of the shock viscosity is small. It is evident from the temperature cuts that the remnant still contains substantial amounts of hot gas when its radius reaches  $100 \text{ pc}$ , so it would be merging with the ISM in the full simulation.

The panels in the right column of Fig. B1 demonstrate that

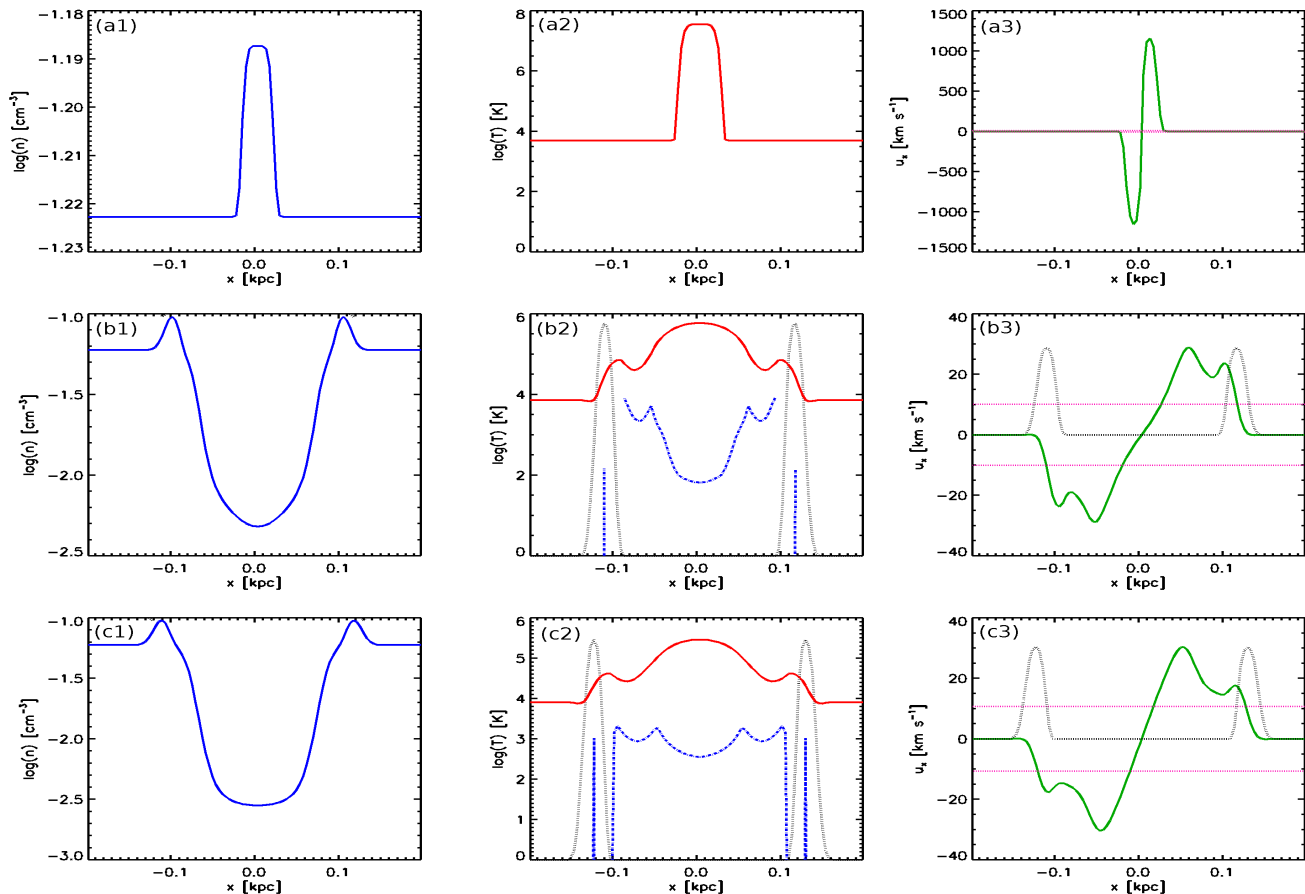


**Figure B2.** One-dimensional cuts through the origin of an SN remnant expanding into gas of ambient density  $\rho_0 = 10^{-25} \text{ g cm}^{-3}$ , simulated with the numerical resolution  $\Delta = 4 \text{ pc}$ . The variables shown are (a1)–(c1) gas number density (blue, solid), (a2)–(c2) temperature (red, solid), and (a3)–(c3) velocity (green, solid). The shock viscosity profile of Eq. (9) (scaled to fit the frame, black, dotted) is shown in the temperature and velocity panels; the net cooling (blue, dashed),  $\log(-T^{-1}(\Gamma - \rho\Lambda)_+)$ , from Eq. (3) is included in the temperature panel; and the ambient sound speed (pink, dotted) is also shown with the velocity. Panels in the top row (a) show the injection profiles used to initialise the remnant at  $t = 0$ ; the lower panel rows are for the later times (b)  $t = 0.72 \text{ Myr}$  and (c)  $t = 1.02 \text{ Myr}$ .

the interior gas velocity can be more than twice the shell speed. Due to the high interior temperature, this flow is subsonic, while the remnant shell expands supersonically with respect to its ambient sound speed. The enhanced viscosity in the hotter interior (with viscosity proportional to the sound speed; see Section 2.4) inhibits numerical instabilities that could arise from the high velocities. In fact, accurate modelling of the SN interiors is not essential in the present context (where we are mainly interested in a realistic description the multi-phase ISM), as long as the interaction of the remnant with the ambient gas is well described, in terms of the energy conversion and transfer to the ISM, the scales and energy of turbulence, and the properties of the hot gas.

## APPENDIX C: BOUNDARY CONDITIONS AND NUMERICAL CONTROL OF ADVECTION AND DIFFUSION

### C1 Top and bottom boundaries

Unlike the horizontal boundaries of the computational domain, where periodic or sliding-periodic boundary conditions are adequate (within the constraints of the shearing box approximation),

the boundary conditions at the top and bottom of the domain are more demanding. The vertical size of the galactic halo is of order of 10 kpc, and nontrivial physical processes occur even at that height, especially when galactic wind and cosmic ray escape are important. As explained in Section 2.4, we do not attempt to model the full extent of the halo here. Therefore, it is important to formulate boundary conditions at the top and bottom of the domain that admit the flow of matter and energy, while minimising any associated artifacts that might affect the interior.

Stress-free, open vertical boundaries would seem to be the most appropriate, requiring that the horizontal stresses vanish, while gas density, entropy and vertical velocity have constant first derivatives on the top and bottom boundaries. These are implemented numerically using ‘ghost’ zones; i.e., three outer grid planes that allow derivatives at the boundary to be calculated in the same way as at interior grid points. The interior values of the variables are used to specify their ghost zone values. When a sharp structure approaches the boundary, the strong gradients are therefore extrapolated into the ghost zones. This artificially enhances the prominence of such a structure, and may cause the code to crash. Here we describe how we have modified these boundary conditions to ensure the numerical stability of our model.

To prevent artificial mass sources in the ghost zones, we im-

pose a weak negative gradient of gas density in the ghost zones. Thus, the density values are extrapolated to the ghost zones from the boundary point as

$$\rho(x, y, \pm Z \pm k\Delta) = (1 - \Delta/0.1 \text{ kpc})\rho(x, y, \pm Z \pm (k-1)\Delta)$$

for all values of the horizontal coordinates  $x$  and  $y$ , where the boundary surfaces are at  $z = \pm Z$ , and the ghost zones are at  $z = \pm Z \pm k\Delta$  with  $k = 1, 2, 3$ . The upper (lower) sign is used at the top (bottom) boundary. This ensures that gas density gradually declines in the ghost zones.

To prevent a similar artificial enhancement of temperature spikes in the ghost zones, gas temperature there is kept equal to its value at the boundary,

$$T(x, y, \pm Z \pm k\Delta) = T(x, y, \pm Z),$$

so that temperature is still free to fluctuate in response to the interior processes. This prescription is implemented in terms of entropy, given the density variation described above.

Likewise, the vertical velocity in the ghost zones is kept equal to its boundary value if the latter is directed outwards,

$$u_z(x, y, \pm Z \pm k\Delta) = u_z(x, y, \pm Z), \quad u_z(x, y, \pm Z) \gtrless 0.$$

However, when gas cools rapidly near the boundary, pressure can decrease and gas would flow inwards away from the boundary. To avoid suppressing inward flows, where  $u_z(x, y, \pm Z) \lesssim 0$  we use the following: if  $|u_z(x, y, \pm Z \mp \Delta)| < |u_z(x, y, \pm Z)|$ , we set

$$u_z(x, y, \pm Z \pm \Delta) = \frac{1}{2} [u_z(x, y, \pm Z) + u_z(x, y, \pm Z \mp \Delta)];$$

otherwise, we set

$$u_z(x, y, \pm Z \pm \Delta) = 2u_z(x, y, \pm Z) - u_z(x, y, \pm Z \mp \Delta).$$

In both cases, in the two outer ghost zones ( $k = 2, 3$ ), we set

$$u_z(x, y, \pm Z \pm k\Delta) = 2u_z(x, y, \pm Z \pm (k-1)\Delta) - u_z(x, y, \pm Z \pm (k-2)\Delta),$$

so that the inward velocity in the ghost zones is always smaller than its boundary value. This permits gas flow across the boundary in both directions, but ensures that the flow is dominated by the interior dynamics, rather than by anything happening in the ghost zones.

The Pencil code is non-conservative, so that gas mass is not necessarily conserved; this can be a problem due to extreme density gradients developing with widespread strong shocks. Solving Eq. (1) for  $\rho$ , rather than  $\ln \rho$ , solves this problem for the snowplough test cases described in Appendix B1, with mass then being conserved within machine accuracy. However for the full model, once the ISM becomes highly turbulent, there remains some numerical mass loss. A comparison of mass loss through the vertical boundaries to the total mass loss in the volume indicates that numerical dissipation accounts for  $\ll 1\%$  per Gyr. The rate of physical loss, from the net vertical outflow, was of order 15% per Gyr.

## C2 Time step control

To achieve numerical stability with the explicit time stepping used, the CFL conditions have to be amply satisfied. For example, for advection terms, the numerical time step should be selected such that

$$\Delta t < \kappa \frac{\Delta}{\max(c_s, u, U)},$$

where  $c_s$  is the speed of sound,  $u = |\mathbf{u}|$  is the amplitude of the perturbed velocity, i.e., the deviation from the imposed azimuthal shear flow  $U$ , and  $\kappa$  is a dimensionless number, determined empirically, which often must be significantly smaller than unity. Apart from the velocity field, other variables also affect the maximum time step, e.g., those associated with diffusion, cooling and heating, so that the following inequalities also have to be satisfied:

$$\Delta t < \frac{\kappa_1 \Delta^2}{\max(\nu, \gamma\chi, \eta)}, \quad \Delta t < \frac{\kappa_2}{H_{\max}},$$

where  $\kappa_1$  and  $\kappa_2$  are further empirical constants and

$$H_{\max} = \max\left(\frac{2\nu|\mathbf{W}|^2 + \zeta_\nu(\nabla \cdot \mathbf{u})^2 + \zeta_\chi(\nabla \cdot \mathbf{u})^2}{c_V T}\right).$$

We use  $\kappa = \kappa_1 = 0.25$  and  $\kappa_2 = 0.025$ . The latter, more stringent constraint has a surprisingly small impact on the typical time step, but a large positive effect on the numerical accuracy. Whilst the time step may occasionally decrease to below 0.1 or 0.01 years following an SN explosion, the typical time step is more than 100 years.

## C3 Minimum diffusivity

Numerical stability also requires that the Reynolds and Péclet numbers defined at the resolution length  $\Delta$ , as well as the Field length, are sufficiently small. These mesh Péclet and Reynolds numbers are defined as

$$\text{Pe}_\Delta = \frac{u\Delta}{\chi} \leq \frac{u_{\max}\Delta}{\chi}, \quad \text{Re}_\Delta = \frac{u\Delta}{\nu} \leq \frac{u_{\max}\Delta}{\nu}, \quad (\text{C1})$$

where  $u_{\max}$  is the maximum perturbed velocity and  $\Delta$  is the mesh length. For stability these must not exceed some value, typically between 1 and 10. Note that the Reynolds and Péclet numbers characterizing the flow are 25 times larger, since  $\Delta = 0.004$  is replaced by  $l_0 \simeq 0.1$  as the relevant turbulent length scale in the non-mesh quantities.

In numerical modelling of systems with weak diffusivity,  $\nu$  and  $\chi$  are usually set constant, close to the smallest value consistent with the numerical stability requirements. This level strongly depends on the maximum velocity, and hence is related to the local sound speed, which can exceed  $1500 \text{ km s}^{-1}$  in our model. To avoid unnecessarily strong diffusion and heat conduction in the cold and warm phases, we scale the corresponding diffusivity with gas temperature, as  $T^{1/2}$ . As a result, the diffusive smoothing is strongest in the hot phase (where it is most required). This may cause reduced velocity and temperature inhomogeneities within the hot gas, and may also reduce the temperature difference between the hot gas and the cooler phases.

The effect of thermal instability is controlled by the Field length,

$$\lambda_F \simeq \left(\frac{KT}{\rho^2 \Lambda}\right)^{1/2} \simeq 2.4 \text{ pc} \left(\frac{T}{10^6 \text{ K}}\right)^{7/4} \left(\frac{n}{1 \text{ cm}^{-3}}\right)^{-1} \left(\frac{\Lambda}{10^{-23} \text{ erg cm}^3 \text{ s}^{-1}}\right)^{-1/2},$$

where we have neglected any heating. To avoid unresolved density and temperature structures produced by thermal instability, we require that  $\lambda_F > \Delta$ , and so the minimum value of the thermal conductivity  $\chi$  follows as

$$\chi_{\min} = \frac{1-\beta}{\gamma\tau_{\text{cool}}} \left(\frac{\Delta}{2\pi}\right)^2,$$

where  $\tau_{\text{cool}}$  is the *minimum* cooling time, and  $\beta$  is the relevant exponent from the cooling function (e.g. as in Table 1 for WSW cooling). In the single remnant simulations of Appendix B,  $\tau_{\text{cool}} \gtrsim 0.75$  Myr. In the full ISM simulations, minimum cooling times as low as 0.05 Myr were encountered.  $\chi_{\text{min}}$  has maxima corresponding to  $\beta = 0.56, -0.2, -3, \dots$  for  $T = 313, 10^5, 2.88 \times 10^5$  K,  $\dots$ . All of these, except for that at  $T = 313$  K, result in  $\chi_{\text{min}} < 4 \times 10^{-4} \text{ km s}^{-1} \text{ kpc}$  at  $c_s = c_1 = 1 \text{ km s}^{-1}$ , so are satisfied by default for any  $\chi_1$  sufficiently high to satisfy the  $\text{Pe}_\Delta \leq 10$  requirement. For  $T = 313$  K, at  $c_s = c_1$  we have  $\chi_{\text{min}} = 6.6 \times 10^{-4} \text{ km s}^{-1} \text{ kpc} > \chi_1$ . Thus if cooling times as short as 0.05 Myr were to occur in the cold gas, we would have  $\lambda_F < \Delta$ , and would be marginally under-resolved. Our analysis of the combined distribution of density and temperature, however, indicates that cooling times this short occur exclusively in the warm gas.

With  $\chi_1 \approx 4.1 \times 10^{-4} \text{ km s}^{-1} \text{ kpc}$ , as adopted in Section 2.4, then  $\text{Pe}_\Delta \leq 10$  is near the limit of numerical stability. (We discuss our choice of thermal diffusivity further in Appendix D.) As a result, the code occasionally crashed (notably when hot gas was particularly abundant), and had to be restarted. When restarting, the position or timing of the next SN explosion was modified, so that the particularly troublesome SN that caused the problem was avoided. In extreme cases, it was necessary to increase  $\chi$  temporarily (for only a few hundred time steps), to reduce the value of  $\text{Pe}_\Delta$  during the period most prone to instability, before the model could be continued with the normal parameter values.

#### APPENDIX D: THERMAL INSTABILITY

One of the two cooling functions employed in this paper, WSW, supports isobaric thermal instability in the temperature range  $313 \leq T < 6102$  K where  $\beta < 1$ . (Otherwise, for the RBN cooling function or outside this temperature range for WSW cooling, we have  $\beta \geq 1$  or  $\Gamma \ll \rho\Lambda$ , so the gas is either thermally stable or has no unstable equilibrium.)

Under realistic conditions of the ISM, thermal instability can produce very small, dense gas clouds which cannot be captured with the resolution  $\Delta = 4$  pc used here. Although the efficiency of thermal instability is questionable in the turbulent, magnetized ISM, where thermal pressure is just a part of the total pressure (Vázquez-Semadeni et al. 2000; Mac Low & Klessen 2004, and references therein), we prefer to suppress this instability in the model. However, we do that not by modifying the cooling function, but rather by enhancing thermal diffusivity so as to avoid the growth of perturbations at wavelengths too short to be resolved by our grid.

Following Field (1965), we introduce the characteristic wave numbers

$$k_\rho = \frac{\mu(\gamma - 1)\rho_0 \mathcal{L}_\rho}{\mathcal{R}c_s T_0}, k_T = \frac{\mu(\gamma - 1)\mathcal{L}_T}{\mathcal{R}c_s}, k_K = \frac{\mathcal{R}c_s \rho_0}{\mu(\gamma - 1)K},$$

where  $\mathcal{R}$  is the gas constant, and the derivatives  $\mathcal{L}_T \equiv (\partial\mathcal{L}/\partial T)_\rho$  and  $\mathcal{L}_\rho \equiv (\partial\mathcal{L}/\partial\rho)_T$  are calculated for constant  $\rho$  and  $T$ , respectively. The values of temperature and density in these equations,  $T_0$  and  $\rho_0$ , are those at thermal equilibrium,  $\mathcal{L}(T_0, \rho_0) = 0$  with  $\mathcal{L} = \rho\Lambda - \Gamma$ . Isothermal and isochoric perturbations have the characteristic wave numbers  $k_\rho$  and  $k_T$ , respectively, whereas thermal conductivity  $K$  is characterised by  $k_K$ .

The control parameter of the instability is  $\varphi = k_\rho/k_K$ .

The instability is suppressed by heat conduction, with the

**Table D1.** The unstable wavelengths of thermal instability, according to Field (1965), at thermally unstable equilibria ( $T_0, \rho_0$ ) with the WSW cooling function.

$T_0$ [K]	$\rho_0$ [ $10^{-24} \text{ g/cm}^3$ ]	$\varphi$	$\lambda_\rho$ [pc]	$\lambda_{\text{cc}}$ [pc]	$\lambda_{\text{mc}}$ [pc]	$\lambda_{\text{cw}}$ [pc]	$\lambda_{\text{mw}}$ [pc]
313	4.97	1.91	2	5	5	2	4
4000	1.20	0.04	101	32	84	14	74
6102	0.94	0.02	192	44	136	20	120

largest unstable wave numbers given by (Field 1965)

$$k_{\text{cc}} = [k_K(k_\rho - k_T)]^{1/2}, \quad (\text{D1})$$

$$k_{\text{cw}} = \left[ -k_K \left( k_T + \frac{k_\rho}{\gamma - 1} \right) \right]^{1/2}, \quad (\text{D2})$$

for the condensation and wave modes, respectively, whereas the most unstable wave numbers are

$$k_{\text{mc}} = \left[ \frac{(1 - \beta)^2}{\gamma^2} + \frac{\beta(1 - \beta)}{\gamma} \right]^{1/4} (k_\rho k_{\text{cc}})^{1/2}, \quad (\text{D3})$$

$$k_{\text{mw}} = \left| \frac{\beta - 1}{\gamma} k_\rho k_{\text{cw}} \right|^{1/2}. \quad (\text{D4})$$

Table D1 contains the values of these quantities for the parameters of the reference model WSWa, where we present the wavelengths  $\lambda = 2\pi/k$  rather than the wave numbers  $k$ . The unstable wavelengths of thermal instability are comfortably resolved at  $T_0 = 6102$  K and 4000 K, with the maximum unstable wavelengths  $\lambda_{\text{cc}} = 44$  pc and 32 pc, respectively, being much larger than the grid spacing  $\Delta = 4$  pc. The shortest unstable wavelength of the condensation mode in our model,  $\lambda_{\text{cc}} = 5$  pc at  $T \approx 313$  K is marginally resolved at  $\Delta = 4$  pc; gas at still lower temperatures is thermally stable. Unstable sound waves with  $\lambda_{\text{cw}} = 2$  pc at  $T = 4000$  K are shorter than the numerical resolution of the reference model. However, for these wave modes to be unstable, the isentropic instability criterion must also be satisfied, which is not the case for  $\beta > 0$ , so these modes remain thermally stable.

Thus, we are confident that the parameters of our models (most importantly, the thermal diffusivity) have been chosen so as to avoid any uncontrolled development of thermal instability, even when only the bulk thermal conductivity is accounted for. Since much of the cold gas, which is most unstable, has high Mach numbers, thermal instability is further suppressed by the shock capturing diffusivity in the cold phase.

#### REFERENCES

- Balsara D. S., Kim J., Mac Low M.-M., Mathews G. J., 2004, ApJ, 617, 339  
 Berkhuijsen E. M., Fletcher A., 2008, MNRAS, 390, L19  
 Berkhuijsen E. M., Fletcher A., 2012, in de Avellez M. A., ed., EAS Publications Series Vol. 56 of EAS Publications Series, Density PDFs of diffuse gas in the Milky Way. pp 243–246  
 Berkhuijsen E. M., Mitra D., Mueller P., 2006, Astron. Nachr., 327, 82  
 Berkhuijsen E. M., Müller P., 2008, A&A, 490, 179  
 Boulares A., Cox D. P., 1990, ApJ, 365, 544  
 Bregman J. N., 1980, ApJ, 236, 577  
 Chiang W.-H., Prendergast K. H., 1985, ApJ, 297, 507  
 Cioffi D. F., McKee C. F., Bertschinger E., 1998, ApJ, 334, 252

- Cox D. P., 2005, *Annu. Rev. Astron. Astrophys.*, 43, 337
- Cox D. P., Smith B. W., 1974, *ApJ*, 189, L105
- de Avillez M. A., 2000, *MNRAS*, 315, 479
- de Avillez M. A., Berry D. L., 2001, *MNRAS*, 328, 708
- de Avillez M. A., Breitschwerdt D., 2004, *A&A*, 425, 899
- de Avillez M. A., Breitschwerdt D., 2005a, *A&A*, 436, 585
- de Avillez M. A., Breitschwerdt D., 2005b, *ApJ*, 634, L65
- de Avillez M. A., Breitschwerdt D., 2007, *ApJ*, 665, L35
- de Avillez M. A., Mac Low M.-M., 2002, *ApJ*, 581, 1047
- Elmegreen B. G., Scalo J., 2004, *ApJ*, 42, 211
- Ferrière K. M., 2001, *Rev. Mod. Phys.*, 73, 1031
- Field G. B., 1965, *ApJ*, 142, 531
- Gaensler B. M., Madsen G. J., Chatterjee S., Mao S. A., 2008, *Publications of the Astronomical Society of Australia*, 25, 184
- Gazol-Patiño A., Passot T., 1999, *ApJ*, 518, 748
- Gent F. A., Shukurov A., Sarson G. R., Fletcher A., Mantere M. J., 2013, *MNRAS*, 430, L40
- Germano M., 1992, *J. Fluid Mech.*, 238, 325
- Gressel O., 2008, PhD thesis, Astrophysikalisches Institut Potsdam
- Gressel O., Elstner D., Ziegler U., Rüdiger G., 2008, *A&A*, 486, L35
- Hanasz M., Kowal G., Otmianowska-Mazur K., Lesch H., 2004, *ApJL*, 605, L33
- Hill A. S., Benjamin R. A., Kowal G., Reynolds R. J., Haffner L. M., Lazarian A., 2008, *ApJ*, 686, 363
- Hill A. S., Joungh M. R., Mac Low M.-M., Benjamin R. A., Haffner L. M., Klingenberg C., Waagan K., 2012, *ApJ*, 750, 104
- Joungh M. K. R., Mac Low M.-M., 2006, *ApJ*, 653, 1266
- Joungh M. K. R., Mac Low M.-M., Bryan G. L., 2009, *ApJ*, 704, 137
- Kalberla P. M. W., Kerp J., 2009, *Annu. Rev. Astron. Astrophys.*, 47, 27
- Korpi M. J., Brandenburg A., Shukurov A., Tuominen I., 1999, *A&A*, 350, 230
- Korpi M. J., Brandenburg A., Shukurov A., Tuominen I., Nordlund Å., 1999, *ApJ*, 514, L99
- Kuijken K., Gilmore G., 1989, *MNRAS*, 239, 605
- Kulkarni S. R., Heiles C., 1987, in Hollenbach D. J., Jr. H. A. T., eds, *Interstellar Processes Vol. 134 of Astrophysics and Space Science Library, The atomic component*. pp 87–122
- Kulkarni S. R., Heiles C., 1988, in Kellermann K. I., Verschuur G. L., eds, *Galactic and Extragalactic Radio Astronomy Neutral hydrogen and the diffuse interstellar medium*. Berlin and New York, Springer-Verlag, pp 95–153
- Mac Low M.-M., Balsara D. S., Kim J., de Avillez M. A., 2005, *ApJ*, 626, 864
- Mac Low M.-M., Klessen R. S., 2004, *Rev. Mod. Phys.*, 76, 125
- McKee C. F., 1995, in Ferrara A., McKee C. F., Heiles C., Shapiro P. R., eds, *Physics of the Interstellar Medium and Intergalactic Medium Vol. 80, The phases of the interstellar medium.*, Astron. Soc. Pacific, San Francisco, p. 292
- McKee C. F., Ostriker J. P., 1977, *ApJ*, 218, 148
- Monin A. S., Yaglom A. M., 2007, *Statistical Fluid Mechanics, Vol. I*, Dover
- Norman C. A., Ikeuchi S., 1989, *ApJ*, 345, 372
- Ostriker J. P., McKee C. F., 1988, *Rev. Mod. Phys.*, 60, 1
- Passot T., Vázquez-Semadeni E., Pouquet A., 1995, *ApJ*, 455, 536
- Putman M. E., Peek J. E. G., Joungh M. R., 2012, *Annu. Rev. Astron. Astrophys.*, 50, 491
- Raymond J. C., Smith B. W., 1977, *ApJ*, 35, 419
- Reynolds R. J., 1977, *ApJ*, 216, 433
- Reynolds R. J., 1991, *ApJL*, 372, L17
- Rosen A., Bregman J. N., 1995, *ApJ*, 440, 634
- Rosen A., Bregman J. N., Kelson D. D., 1996, *ApJ*, 470, 839
- Rosen A., Bregman J. N., Norman M. L., 1993, *ApJ*, 413, 137
- Sánchez-Salcedo F. J., Vázquez-Semadeni E., Gazol A., 2002, *ApJ*, 577, 768
- Sarazin C. L., White III R. E., 1987, *ApJ*, 320, 32
- Scalo J., Vázquez-Semadeni E., Chappell D., Passot T., 1998, *ApJ*, 504, 835
- Slyz A. D., Devriendt J. E. G., Bryan G., Silk J., 2005, *MNRAS*, 356, 737
- Spitzer Jr. L., 1990, *Annu. Rev. Astron. Astrophys.*, 28, 71
- Tammann G. A., Löffler W., Schröder A., 1994, *ApJS*, 92, 487
- Tennekes H., Lumley J. L., 1972, *First Course in Turbulence*. Cambridge: MIT Press
- Vázquez-Semadeni E., 2012, in de Avillez M. A., ed., *EAS Publications Series Vol. 56 of EAS Publications Series, Are There Phases in the ISM?*. pp 39–49
- Vázquez-Semadeni E., Garcia N., 2001, *ApJ*, 557, 727
- Vázquez-Semadeni E., Gazol A., Scalo J., 2000, *ApJ*, 540, 271
- Vázquez-Semadeni E., Passot T., Pouquet A., 1995, *ApJ*, 441, 702
- Wada K., Meurer G., Norman C. A., 2002, *ApJ*, 577, 197
- Wada K., Norman C. A., 1999, *ApJ*, 516, L13
- Wada K., Norman C. A., 2001, *ApJ*, 547, 172
- Wada K., Norman C. A., 2007, *ApJ*, 660, 276
- Wakker B. P., van Woerden H., 1997, *Annu. Rev. Astron. Astrophys.*, 35, 217
- Walters M. A., Cox D. P., 2001, *ApJ*, 549, 353
- Wisdom J., Tremaine S., 1988, *AJ*, 95, 925
- Wolfire M. G., Hollenbach D., McKee C. F., Tielens A. G. G. M., Bakes E. L. O., 1995, *ApJ*, 443, 152
- Woltjer L., 1972, *Annu. Rev. Astron. Astrophys.*, 10, 129